



Lunar-forming impacts: High-resolution SPH and AMR-CTH simulations

R.M. Canup^{a,*}, A.C. Barr^{a,b}, D.A. Crawford^c

^a Southwest Research Institute, Planetary Science Directorate, United States

^b Brown University, Department of Geological Sciences, United States

^c Sandia National Laboratories, United States

ARTICLE INFO

Article history:

Received 22 March 2012

Revised 16 October 2012

Accepted 19 October 2012

Available online 5 November 2012

Keywords:

Moon

Satellites, Formation

Planetary formation

Impact processes

ABSTRACT

We present results of the highest-resolution simulations to date of potential Moon-forming impacts using a Lagrangian, particle-based method (smooth particle hydrodynamics, or SPH) and an Eulerian, grid-based method with adaptive mesh refinement (AMR-CTH). We consider a few candidate impacts advocated by recent works, directly comparing simulations performed at varying resolutions and with both numerical methods and their predictions for the properties of resulting protolunar disks. For a fixed set of impact conditions, simulations with either method and with different resolutions yield very similar results for the initial impact and the first few hours of the post-impact period. The subsequent disk properties in the ~5–20 h time period can vary substantially from case-to-case, depending on the orbits of and mutual interactions between large bound clumps of ejecta that often form after the initial impact. After such clumps have completed at least one orbit (which typically requires ~25–50 h), the predicted protolunar disk mass and its angular momentum converge to within about 10% for simulations of very similar impact conditions using different resolutions or methods. The disks produced by the CTH simulations are consistently about 10% less massive than those produced by SPH simulations, due presumably to inherent differences between the codes. The two methods predict broadly similar values for the fraction of the protolunar disk that originates from the target vs. the impactor, and for the initial disk radial surface density and temperature profiles.

© 2012 Elsevier Inc. All rights reserved.

1. Background

The giant impact theory proposes that the Moon formed from material ejected when a roughly Mars-sized protoplanet obliquely impacted the Earth (e.g., Cameron and Ward, 1976; Benz et al., 1989; Canup and Asphaug, 2001). Forming Earth-sized planets is thought to require collisions between large protoplanetary embryos (e.g., Chambers and Wetherill, 1998), so that giant impacts should have been common during the final stage of terrestrial planet accretion (e.g., Agnor et al., 1999). The impact theory is favored because it can account for multiple aspects of the Earth–Moon system. A large, oblique impact provides a straightforward explanation for the high angular momentum of the Earth–Moon system, which implies that the Earth rotated with an approximately 5 h day when the Moon orbited close to the Earth. An oblique impact by a differentiated impactor can also produce a disk that is highly depleted in iron, providing an explanation for the low lunar bulk density (e.g., Benz et al., 1989; Canup and Asphaug, 2001).

Despite its strengths, there remain several aspects of the giant impact theory that are not obviously consistent with observed

properties of the Moon. The Moon shares several distinct compositional similarities to the Earth's mantle, including identical oxygen, tungsten, and silicon isotope compositions (e.g., Wiechert et al., 2001; Touboul et al., 2007; Georg et al., 2007). Such similarities could naturally result if the protolunar disk originated from material derived overwhelmingly from the target protoearth. Prior hydrodynamical simulations have generally predicted the opposite: a protolunar disk derived primarily from material originating in the impactor. It appears unlikely that an impactor would have had an identical oxygen composition to that of the Earth given the degree of radial mixing predicted by terrestrial accretion simulations and assuming that the observed difference in the O-isotope compositions of Earth and Mars is indicative of the general variation of O-isotope composition with position in the solar nebula (Pahlevan and Stevenson, 2007). However an impactor composition identical to that of the Earth cannot be ruled out; e.g., Belbruno and Gott (2005) argue that an impactor forming at the same semi-major axis as the Earth could have had an Earth-like composition.

An alternative has been proposed by Pahlevan and Stevenson (2007), who suggest that the silicate vapor component of the inner protolunar disk diffusively mixed with vaporized portions of the upper Earth soon after the giant impact. This would allow the disk to achieve a terrestrial composition even if it was originally derived

* Corresponding author. Address: Southwest Research Institute, 1050 Walnut Street, Suite 300, Boulder, CO 80302, United States.

E-mail address: robin@boulder.swri.edu (R.M. Canup).

primarily from an impactor of different composition than the Earth. The equilibration scenario appears to require that the Moon's accumulation is delayed by 100 years or more after the impact, and that most of the material that ends up in the Moon, which itself accumulates in the outer regions of the disk, is processed through the inner disk where it can equilibrate with the Earth. Whether both of these constraints can be satisfied depends in part on the initial distribution of disk material, because more radially distant material orbiting exterior to the Roche limit will tend to accumulate rapidly and be less likely to equilibrate (e.g., Salmon and Canup, 2012).

A second potential issue with the giant impact theory concerns water. Recent works (e.g., Saal et al., 2008; Hauri et al., 2011) suggest that at least portions of the very early Moon had Earth-like abundances of water, which is at odds with a longstanding view that a highly energetic impact event would result in widespread volatile loss. It however may be possible to retain some water in the protolunar disk, depending on disk conditions (Desch and Taylor, 2011).

Open questions such as these motivate continued study of potential Moon-forming impacts. Our purpose here is to assess the effects of numerical method and resolution on the outcomes of impact simulations, focusing on the predicted properties of the resulting protolunar disks, including their masses, angular momenta, radial surface density and temperature profiles, and impactor vs. target compositions. In Section 2, we review basic constraints on a potential Moon-forming impact (see also Canup, 2004a,b for discussion). Section 3 describes our numerical methods. Simulation results are presented in Section 4, followed by a discussion in Section 5.

2. Constraints and trends in impact outcome

The lunar forming impact was probably the last major event in Earth's accretion. In the simplest case, the impact leaves an approximately Earth-mass planet, together with a planet-disk pair whose total angular momentum is comparable to that in the current Earth–Moon system, $L_{EM} \equiv 3.5 \times 10^{41} \text{ g cm}^2 \text{ s}^{-1}$. A successful candidate impact must also produce a protolunar disk with sufficient mass and angular momentum to eventually accumulate into a Moon of mass $M_L = 0.012M_{\oplus} = 7.35 \times 10^{25} \text{ g}$ exterior to the Earth's Roche limit, which is located at a distance $a_R \sim 2.9R_{\oplus}$ for lunar density material, where R_{\oplus} is the radius of the Earth. Prior N -body simulations of lunar accretion from an impact-generated disk find the most likely outcome is a single large Moon with semi-major axis $a \approx 1.3a_R$, with inner disk material driven into the planet by gravitational interactions with the Moon (Ida et al., 1997; Kokubo et al., 2000). Such models indicate that the material initially in the protolunar disk typically ends up in one of three places: (1) it is accreted into a Moon with $a = \lambda a_R$, (2) it is accreted by the Earth, or (3) it escapes the Earth–Moon system. A mass and angular momentum conservation argument can then be used to estimate the mass of the Moon that would accumulate from the disk as a function of the initial disk mass (M_D), the initial disk angular momentum (L_D), the position of the Moon (λ), and the angular momentum of material that escapes or collides with the Earth. Based on results of N -body simulations and assuming $\lambda = 1.3$, the predicted Moon mass is

$$\frac{M_M}{M_D} \approx 1.9 \left(\frac{L_D}{M_D \sqrt{GM_{\oplus} a_R}} \right) - 1.1 - 1.9 \left(\frac{M_{esc}}{M_D} \right) \quad (1)$$

where M_{esc} is the mass that escapes as the disk evolves and the Moon accretes, with typically $M_{esc} \leq 0.05M_D$ (Ida et al., 1997; Kokubo et al., 2000). The first term in parentheses on the right hand side of Eq. (1) is the disk's specific angular momentum, scaled to the specific angular momentum of a circular orbit with $a = a_R$; as

in prior works we define this quantity as $j_{disk} \equiv L_D/[M_D(GM_{\oplus}a_R)^{1/2}]$. Eq. (1) provides a simple means for evaluating whether a given impact-generated disk predicted by a hydrodynamical simulation could later yield a lunar-mass Moon. It is physically invalid for cases that would give $M_M/M_D > 1$; these correspond to initial disks with specific angular momenta too high to be consistent with the assumptions in Eq. (1), primarily that the final Moon forms with $a = 1.3a_R$. For $M_{esc} = 0$, Eq. (1) predicts $M_M/M_D > 1$ for $j_{disk} > 1.1$; for such cases we set $M_M = M_D$. In addition, equation (1) overestimates the Moon's mass if the Moon's initial semi-major axis is substantially larger than $a = 1.3a_R$, which appears probable based on recent modeling by Salmon and Canup (2012).

It has generally been assumed that the impact must produce a disk whose iron content is no greater than the bulk mass abundance of elemental iron in the Moon, believed to be in the few to 10% range (e.g., Benz et al., 1987; Canup and Asphaug, 2001; Canup, 2004a and references therein). In the equilibration scenario of Pahlevan and Stevenson (2007), iron in the inner disk would tend to be diluted through mixing with the iron-depleted layers of the upper Earth after the impact (Pahlevan et al., 2011), and so it is possible that in this case the requirement of iron-depletion in the inner disk may be relaxed.

The angular momentum in the Earth–Moon system is known to have decreased by of order $10^{-2} L_{EM}$ over its history due to tides raised on the Earth by the Sun that slow the Earth's rotation (e.g., Canup et al., 2001). The magnitude of this change is constrained by the time averaged tidal parameters for the Earth, which are in turn constrained by the requirement that the Moon evolved to its current orbital distance in 4.5 byr. Additional angular momentum would have been removed by material escaping from the protolunar disk during lunar accretion (this likely would have been of order a few $\times 10^{-2} L_{EM}$; Kokubo et al., 2000; Salmon and Canup, 2012), or if the Moon was captured into the evection resonance with the Sun and driven to a high eccentricity orbit (Touma and Wisdom, 1998; Canup, 2008; Ćuk and Stewart, 2012). We here focus on impacts that leave a bound planet-disk system whose total angular momentum, L_F , is comparable to that in the current Earth–Moon, with $1 \leq L_F/L_{EM} \leq 1.2$.

If the target protoearth and impactor are objects of mean density ρ that are not rotating prior to their collision, the angular momentum delivered by an impactor of mass $M_i \equiv \gamma M_T$ is

$$\begin{aligned} L_{col} &= b' M_T^{5/3} f(\gamma) \sqrt{\frac{2G}{4\pi\rho/3}} \left(\frac{v_{imp}}{v_{esc}} \right) \\ &\approx 1.3 L_{EM} b' \left(\frac{M_T}{M_{\oplus}} \right)^{5/3} \left(\frac{\gamma}{0.1} \right) \left(\frac{v_{imp}}{v_{esc}} \right) \end{aligned} \quad (2)$$

where $b' \equiv \sin(\xi)$ is the scaled impact parameter, ξ is the angle between the surface normal and the impact trajectory (so that a grazing impact has $b' = 1$ and $\xi = 90^\circ$), M_T is the total colliding mass (impactor + target), γ is the impactor-to-total mass ratio, $f(\gamma) \equiv \gamma(1-\gamma)\sqrt{\gamma^{1/3} + (1-\gamma)^{1/3}}$, (v_{imp}/v_{esc}) is the ratio of the impact velocity to the mutual escape velocity, and $v_{imp}^2 = v_{esc}^2 + v_{\infty}^2$, where v_{∞} is the relative velocity of the target and impactor at large separation.

General trends in impact outcome as a function of b' , (v_{imp}/v_{esc}) , and γ have been observed (e.g., Canup et al., 2001; Canup and Asphaug, 2001; Agnor and Asphaug, 2004; Canup, 2004a, 2008; Asphaug, 2010; Leinhardt and Stewart, 2012). For oblique, high-velocity impacts (with $b' > 0.7$ and $(v_{imp}/v_{esc}) \geq 1.2$), most of the impactor escapes and little mass is left in an orbiting disk (Agnor and Asphaug, 2004). For low-velocity impacts (i.e., $(v_{imp}/v_{esc}) \leq 1.1$), the disk mass generally increases as b' is increased, because increasing b' leads to a larger portion of the impactor grazing past the target where it can most effectively be

subject to gravitational torques that allow it to achieve bound Earth orbit (e.g., Canup, 2008). While low-velocity collisions with $b' > 0.75$ produce massive disks, they have previously been thought too iron rich to yield the Moon (although see above). For a fixed M_T , b' and (v_{imp}/v_{esc}) , increasing the impactor mass fraction γ typically increases the final disk mass. A target protoearth with a pre-impact retrograde rotation (i.e. in the opposite rotational sense as the impact itself) allows for somewhat larger impactors for the same total angular momentum; such collisions have been found to produce massive disks and an improved match with the Earth–Moon system angular momentum compared to those involving non-rotating targets (Canup, 2008). Conversely, a target with a rapid prograde rotation before the collision generally leads to disks that are not massive enough to produce the Moon when the constraint that

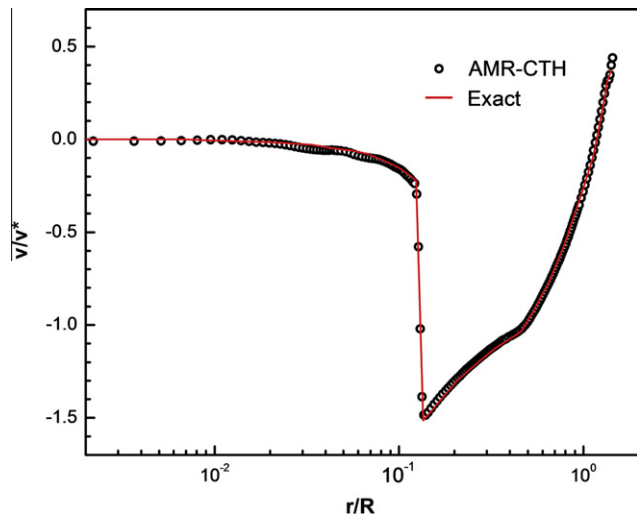


Fig. 1. Adiabatic collapse of an initially isothermal spherical gas cloud. Comparison of the exact solution from Steinmetz and Müller (1993) with AMR-CTH using the equal mass approximation is shown at $t/t^* \sim 0.77$.

the final system angular momentum must be $\sim L_{EM}$ is applied (Canup, 2008).

With or without pre-impact rotation, most of the lunar-forming cases previously identified have $0.11 \leq \gamma \leq 0.2$, low impact velocities with $(v_{imp}/v_{esc}) \leq 1.1$, and moderate impact parameters, $0.65 < b' < 0.75$, corresponding to impact angles between about 40° and 50° . Because 45° is the most probable impact angle for randomly oriented impacts, $\sim 15\%$ of all collisions have $40^\circ \leq \xi \leq 50^\circ$. Such impacts that produce disks massive enough to yield the Moon have disks derived primarily (60–90%) from the impactor's mantle (Canup, 2004a, 2008).

Less oblique ($b' \sim 0.5$ – 0.6), higher velocity collisions can also produce substantial disks. In such cases the loss of mass and angular momentum during the impact can be significant, so that L_{col} can be substantially greater than L_{EM} and still leave a final bound system whose angular momentum is $\sim L_{EM}$. Canup (2008, Fig. 1) found that collisions with $\gamma = 0.13$, $1.2 \leq (v_{imp}/v_{esc}) \leq 1.4$, and $0.5 < b' < 0.65$ produced disks with $0.3M_L < M_D < 0.9M_L$ that contained 30% to 70% impactor material by mass. Some of these disks thus originated predominantly from the target rather than from the impactor, although they were not considered successful because they did not contain enough mass to produce the Moon (i.e., they had $M_M < M_L$ from Eq. (1), even in the limit that $M_{esc} = 0$). Recent simulations by Reufer et al. (2011, 2012) have explored similar types of collisions including larger impactors and higher impact speeds. They advocate a $v_{imp} \sim 1.2$ – $1.3v_{esc}$, $b' = 0.5$ – 0.6 , and $\gamma \sim 0.2$ impact as one that can produce a disk with roughly a lunar mass and with a reduced percentage of impactor-derived material (~ 40 – 45%).

The majority of our simulations here consider low velocity, oblique impacts (both with and without pre-impact rotation in the target as in Canup, 2004a, 2008), but we also include a head-on, higher velocity collision as advocated by Reufer et al. (2011).

3. Methods

Hydrodynamical models of giant impacts have primarily used smooth particle hydrodynamics, or SPH (e.g., Benz et al., 1986,

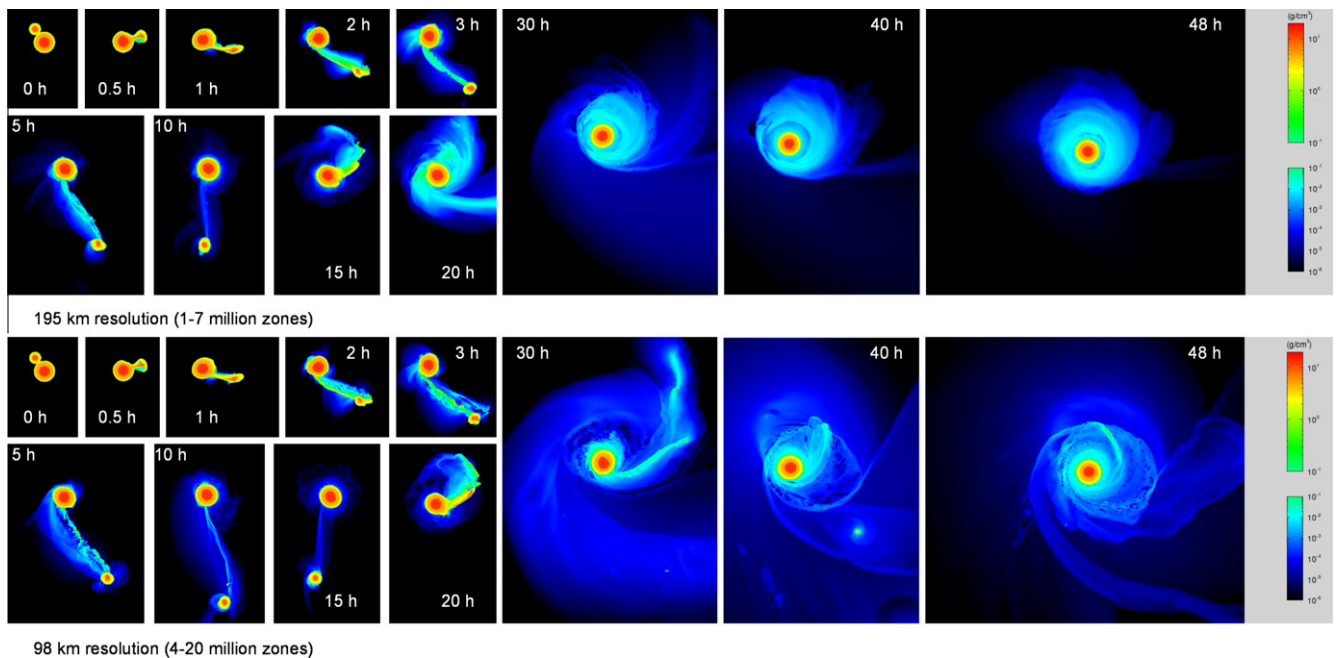


Fig. 2. AMR-CTH simulations of the same impact at two resolutions. The collision occurs in the clockwise direction. Color scales logarithmically with density in g cm^{-3} , with black to dark red corresponding to $10^{-6} \text{ g cm}^{-3}$ to about 20 g cm^{-3} , respectively. Shown below each sequence is the smallest grid cell width used in the AMR scheme and the approximate total number of grid cells used in the calculation.

1987, 1989; Canup and Asphaug, 2001; Canup, 2004a, 2008). SPH represents matter as particles whose individual evolutions due to gravity, pressure forces, and shock dissipation are calculated as a function of time. The Lagrangian formulation of SPH is well suited to tracking different materials and particle histories (e.g., whether the mass in the protolunar disk originated from the impactor or the target). SPH is a computationally efficient method for modeling large impacts, because the code's numerical resolution follows the evolution of the colliding material as it disperses through a large total volume of space.

Eulerian grid-based models have also been applied to lunar forming collisions in a few instances. Melosh and Kipp (1989) modeled the first hour of a giant impact in 3-D using an early version of the Eulerian shock physics code CTH specially modified to include a radial gravity body force. The first three-dimensional Eulerian model using explicit self-gravity was applied to lunar-forming impacts by Wada et al. (2006). Their simulations utilized a fixed grid, did not consider multiple materials (so that mantle vs. core material were not distinguished), and were extremely computationally intensive. They considered two equations of state for the colliding planets. The first (EOS-1) corresponded to an ideal gas at high temperatures and a polytrope at low temperatures, and was intended to represent vaporized material. The second (EOS-2) was a Tillotson-like equation of state that treated the material as a fluid. Two impact simulations using EOS-1 showed strong shocks in the disk (e.g., their Fig. 1) and did not ultimately produce disks massive enough to yield the Moon. Wada et al. argued that in these cases, efficient angular momentum transport across the spiral shock structures caused the majority of the disk material to rapidly accrete onto the Earth, e.g., within the first 20 h. However it is not clear that EOS-1 was realistic: the colliding planets would have been fluid-like (rather than vapor-like) prior to their collision, and more sophisticated equations of state predict that only of order 10–30% of the disk mass is vaporized by a low-velocity impact of a Mars-sized impactor (e.g., Canup, 2004a and Section 4.1.2), suggesting that EOS-2 would be a more appropriate treatment. The two Wada et al. simulations using EOS-2 showed the impactor material dispersed into condensed strips of disk material (e.g., their Fig. 4), qualitatively similar to results seen in prior SPH simulations. The one Wada et al. simulation using both EOS-2 and a grid large enough to contain most of the orbiting disk material ($40R_{\oplus} \times 40R_{\oplus} \times 10R_{\oplus}$) found a predicted satellite mass broadly comparable to that determined using SPH for similar collisions (i.e., the thin solid line in their Fig. 5).

Recently CTH has been adapted to include self-gravity and adaptive meshing (Crawford et al., 2006), and the latter increases computational speed greatly compared to fixed grid methods (Canup and Barr, 2010; Crawford and Kipp, 2010; Crawford, 2011a). We here utilize both SPH and this version of AMR-CTH, described next.

3.1. P-SPH

In SPH, material is described by a large number of spherically symmetric particles, each of which represents a quantity of mass of a given composition. The 3-D spatial distribution of each particle is defined with a density weighting function, known as the kernel, and a characteristic radius, known as the smoothing length, h . The functional form of the kernel does not change during a simulation, but the smoothing length of each particle is varied so as to maintain overlap with a desired number of other particles (typically a few tens). This allows low-density regions to be smoothly resolved, although with coarse spatial resolution.

In the version of SPH used here (a descendant of that of W. Benz), the evolution of each particle's position, velocity, internal energy and density are evolved due to gravity, compressional heating and expansional cooling, and shock dissipation. Material

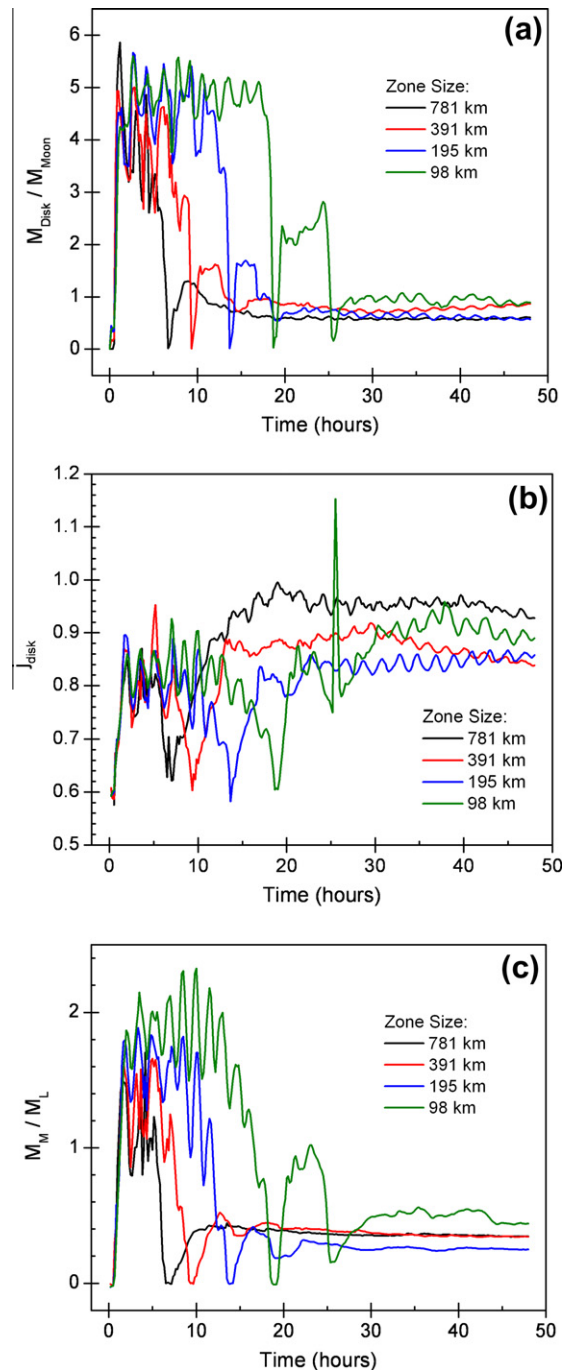


Fig. 3. Time evolution of the orbiting disk mass in lunar masses (a), the disk specific angular momentum, normalized to that of an orbit at the Roche limit (b), and the predicted mass of the resulting Moon from Eq. (1) in lunar masses (c) for the impact shown in Fig. 2. AMR-CTH results are shown at four resolutions, with the highest two resolutions (blue and green curves) corresponding to the cases in Fig. 2.

strength is ignored. The equation of state relates a particle's specific internal energy and local density to pressure at each time step. A tree code is used for the gravity calculations, in which the force exerted by distant particles is approximated by a low-order multipole expansion. A group of particles of extent l is considered distant if the distance to its center of mass, D , satisfies $D > l/\theta$, where θ is an accuracy parameter of order unity (e.g., Crawford, 2011b), which is set to $\theta = 0.65$ in our SPH simulations.

We use a parallelized version of SPH that allows for million-particle simulations, an order-of-magnitude increase compared to Can-

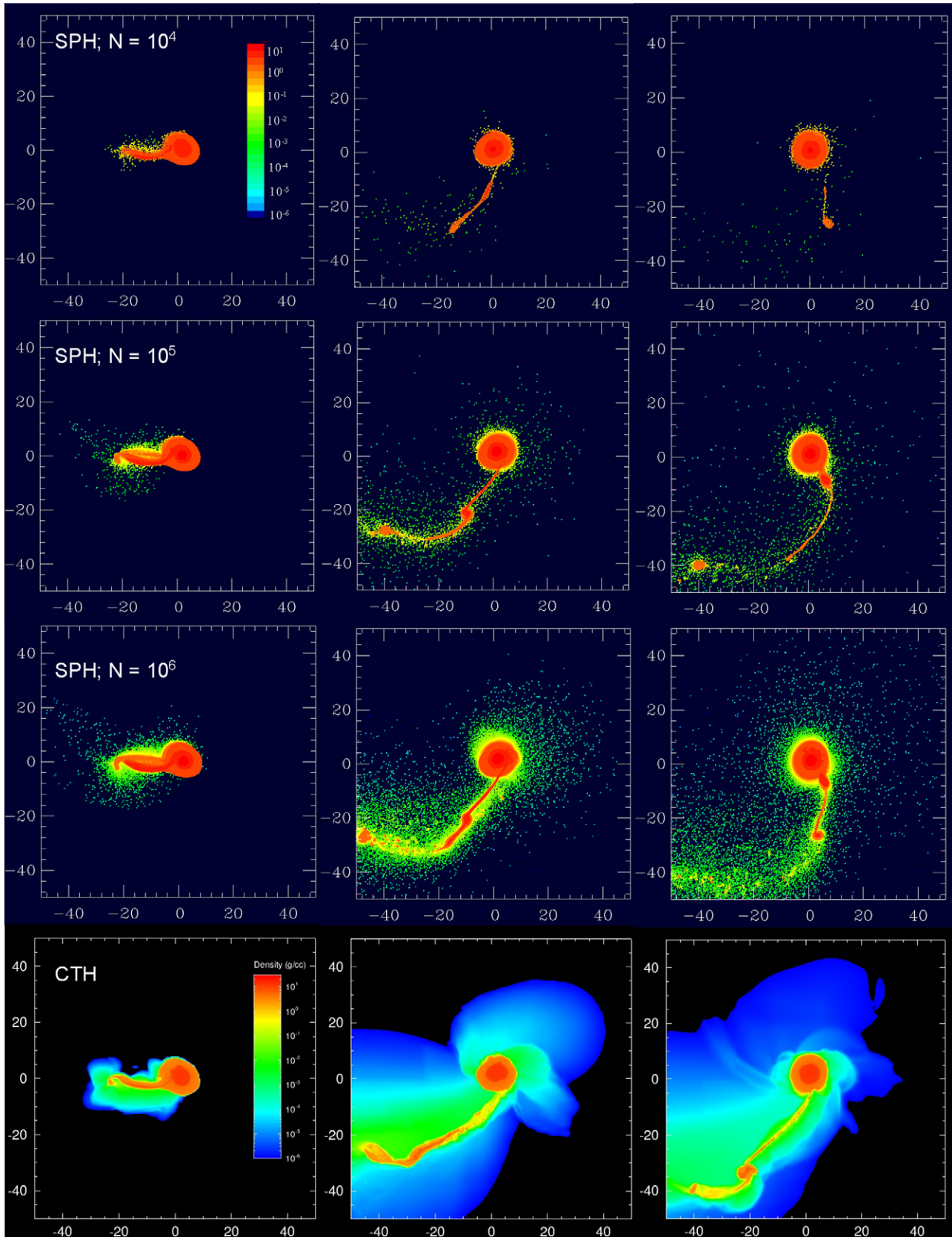


Fig. 4. page 1: SPH simulations with $N = 10^4$ (top row), 10^5 (second row), and 10^6 (third row) particle resolution, compared with a CTH simulation (bottom row) with a 198 km minimum cell size. The collision is a low-velocity, oblique impact comparable to that in Fig. 2 of Canup (2004a), with $\gamma = 0.13$, $v_{\text{imp}} = v_{\text{esc}}$, $b' = 0.72$, $L_T \sim 1.25L_{EM}$, and no pre-impact spin. Color scales logarithmically with density, per color bars in first SPH and CTH frames, with dark blue to deep red corresponding to $10^{-6} \text{ g cm}^{-3}$ to about 20 g cm^{-3} , respectively. Values for all SPH particles are overplotted in order of increasing density (so that the highest density values are plotted on top, allowing for easiest comparison with the CTH results), while CTH images show the density in the midplane. Columns left to right correspond to $t = 1, 3.8,$ and 5.4 h. Fig. 4, page 2: Columns left to right correspond to $t = 8.6, 24.7,$ and 49.5 h (for the SPH simulations) and 40.3 h (for the CTH simulation).

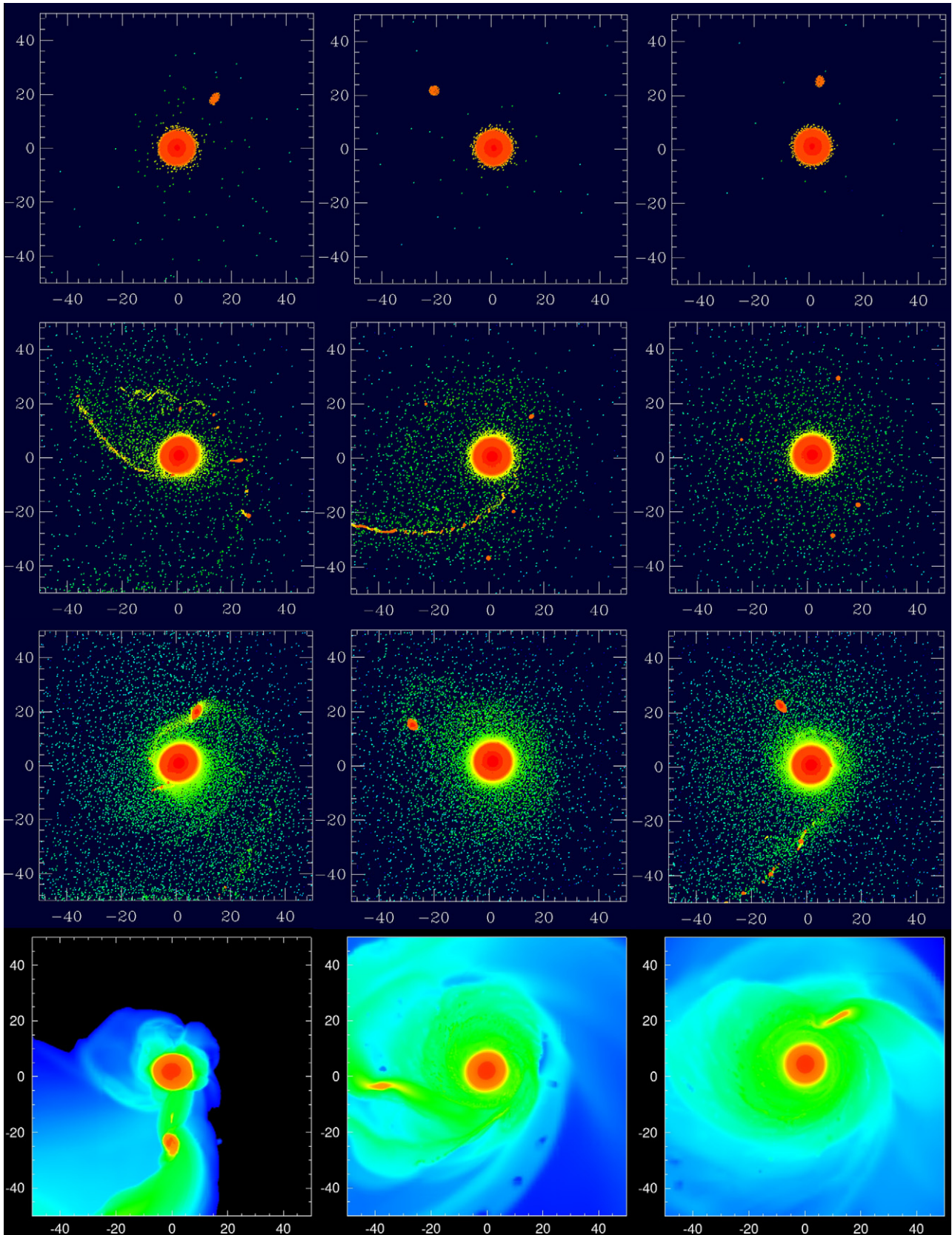


Fig. 4. (continued)

up (2004a, 2008). Even with the parallelized code, each 10^6 -particle simulation required more than 2 months on a dedicated eight-node cluster. Increasing N slows the calculation in two ways: (1) the num-

ber of gravitational force and nearest neighbor calculations that must be performed at each time step is increased, and (2) the increased spatial resolution requires smaller time steps to satisfy the

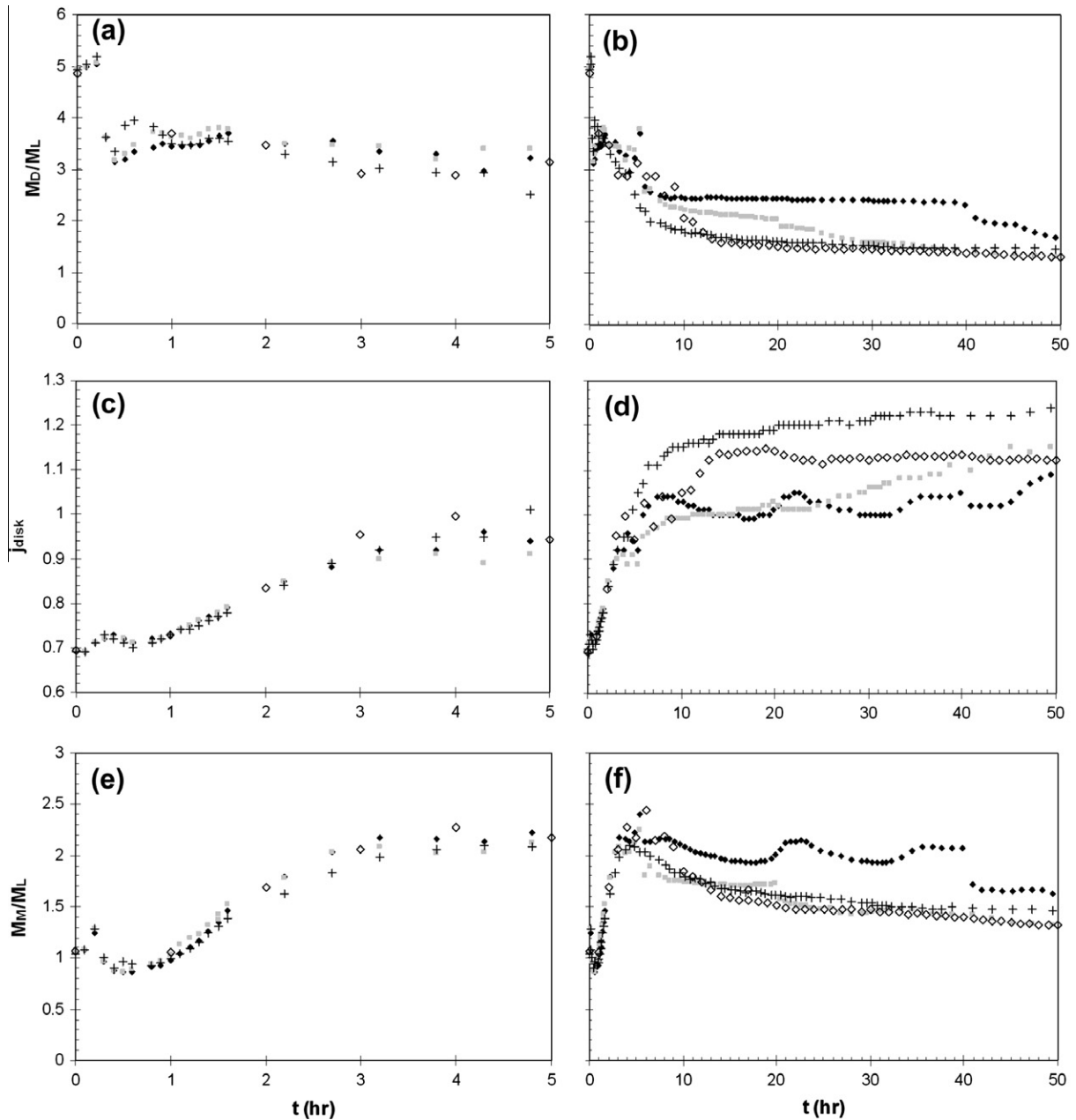


Fig. 5. Results of SPH simulations with several resolutions ($N = 10^4$, crosses; $N = 10^5$, gray squares; and $N = 10^6$, black filled diamonds) and a CTH simulation (open diamonds) of the impact shown in Figs. 4 and 6. Plots show the orbiting disk mass in lunar masses (a and b), the disk specific angular momentum, normalized to that of an orbit at the Roche limit (c and d), and the predicted mass of the resulting Moon from Eq. (1) in lunar masses (e and f) for the first 5 simulated hours (left) and the full 50 simulated hours (right).

Courant condition, which requires that the time step be smaller than the sound speed crossing time across the smallest SPH particle.

The colliding objects are assumed to be differentiated, with each containing 30% iron and 70% mantle (dunite/forsterite) by mass, and are generated with an initially uniform spacing between SPH particles. The surface temperatures of both the impactor and the target are initially set to ~ 2000 K, with temperatures increasing along an adiabat with increasing depth (as in Canup, 2004a). The objects are then simulated in isolation for about 10 h, allowing them to settle to a hydrostatically equilibrated state prior to the collision.

3.2. AMR-CTH

We also simulate impacts with CTH (McGlaun et al., 1990), a well-known code widely used to model smaller-scale planetary

impacts (e.g., Pierazzo et al., 1997, 2008). We use CTH version 9.1 with self-gravity implemented using a tree code (Barnes and Hut, 1986) with $\theta = 0.75$, the M-ANEOS equation of state (see Section 3.3 and Appendix A), and adaptive mesh refinement (AMR) (see, e.g., Crawford and Kipp, 2010). AMR allows for high resolution in high-density regions of the domain, while low density regions are coarsely resolved. We adopt an equal mass approximation refinement scheme, using a factor of 2 larger cell width when the density decreases by a factor of 8; this produces nearly equal mass zones, which coarsely mimics the fixed mass particles of SPH. Input parameters then specify the smallest and largest allowed cell sizes.

As a verification test for the new AMR-CTH code, we model the adiabatic collapse of an initially isothermal sphere. We consider an ideal gas (polytropic index $5/3$) sphere of mass M and radius R with a density distribution, $\rho(r) = M/(2\pi r R^2)$, where r is distance from

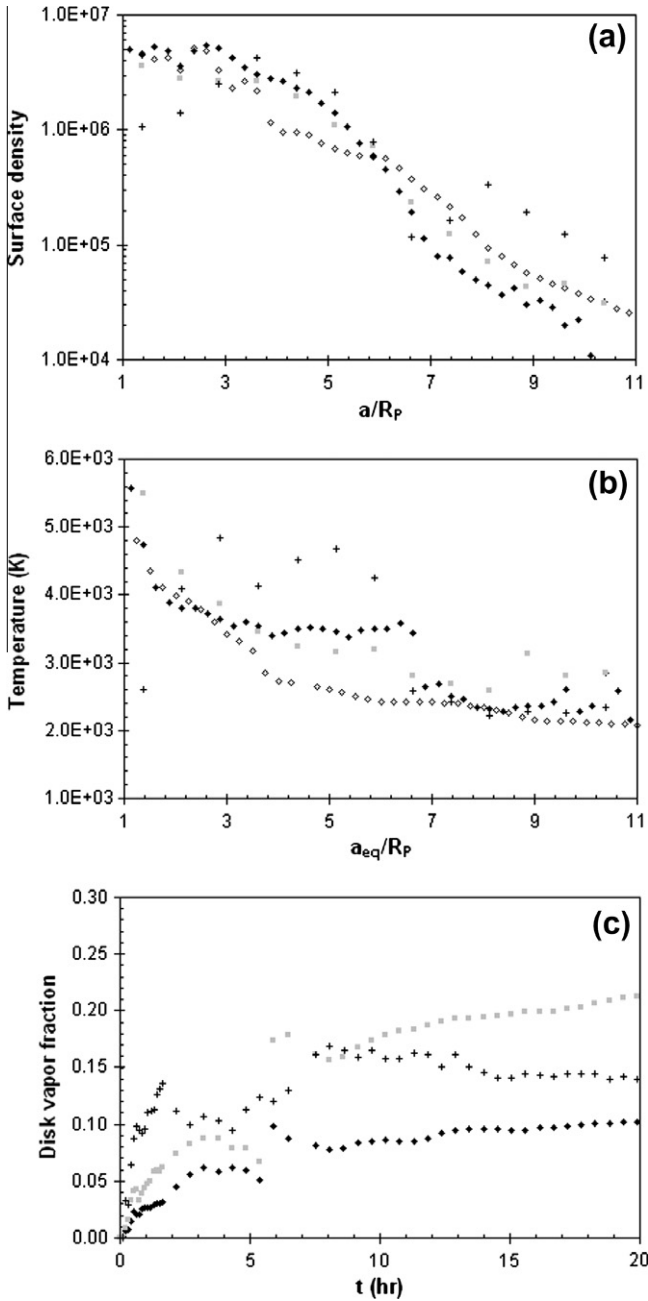


Fig. 6. The predicted disk surface density disk in g cm^{-2} (a) and the disk temperature (b) computed at $t = 50$ h as a function of the equivalent circular orbit of each orbiting particle/cell. Shown are results of SPH simulations ($N = 10^4$, crosses; $N = 10^5$, gray squares; $N = 10^6$, black filled diamonds) and a CTH simulation (open diamonds) of the impact described in Section 4.2. In the $N = 10^4$ SPH simulation, the majority of the disk material (75%) is contained in a single intact clump with $a_{\text{eq}} \sim 4R_p$. Frame (c) shows the evolution of the disk vapor fraction vs. time in the SPH simulations.

the sphere's center. With a uniform initial internal specific energy, u , that is 5% of the characteristic gravitational energy, i.e. $u = 0.05GM/R$, the sphere collapses, producing shocks and rarefactions. This problem has been extensively studied in one dimension using Lagrangian finite element methods with sufficient accuracy to be considered exact (e.g., Steinmetz and Müller, 1993). Results are typically expressed in dimensionless form normalized to a characteristic density, $\rho^* = 3M/4\pi R^3$, time, $t^* = (R^3/GM)^{1/2}$ and velocity, $v^* = (GM/R)^{1/2}$. The test case shown in Fig. 1 produces excellent agreement with the exact solution.

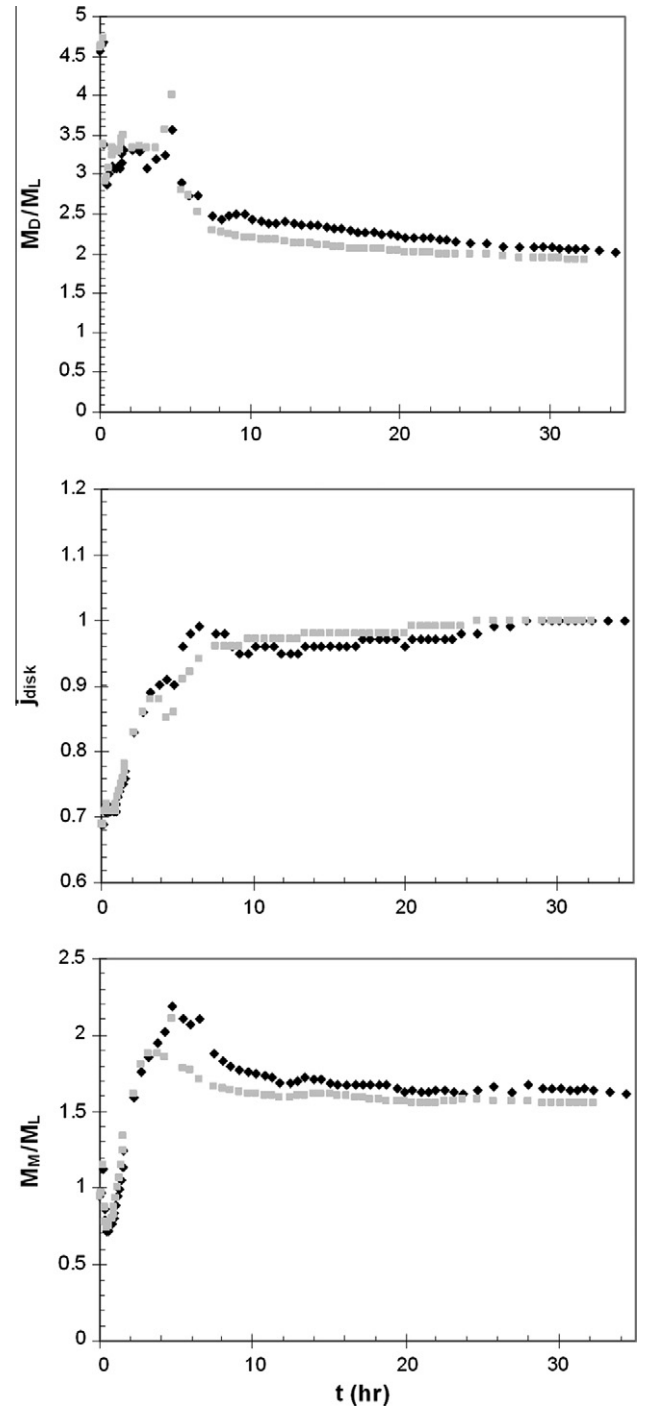


Fig. 7. Same collision and quantities as in Fig. 5, only here with a target that had a slow, prograde spin prior to the collision. SPH simulation results shown for two resolutions ($N = 10^5$, gray squares; $N = 10^6$, black diamonds).

3.3. M-ANEOS equation of state

Our SPH and AMR-CTH simulations use the semi-analytic equation of state known as ANEOS (Thompson and Lauson, 1972). In ANEOS, thermodynamic quantities are derived from the Helmholtz free energy, F , described as a sum of three components: a zero-temperature free energy, a nuclear component, and an electronic ionization term. The nuclear component is determined via an interpolation function that approximates a crystalline Debye solid at low temperatures and an ideal gas at high temperatures. ANEOS

computes temperature (as opposed to only specific internal energy, as is typical in simpler equations of state), as well as the mass fraction contained in each phase for mixed phase states. In SPH, each particle represents a single material, and mixed phase states (e.g., a two-phase vapor and melt) are described by treating the different phases as separate components that are in temperature and pressure equilibrium. In CTH, a single cell can contain different materials and/or void space. In mixed materials cells, each material has its own thermodynamic state (mass, energy, temperature, pressure) and contributes to average cell properties (temperature, pressure) with a weighted average, where temperature is weighted by heat capacity and pressure is weighted by volume.

The classic ANEOS equation of state (Thompson and Lauson, 1972) treats vapor as monatomic, which requires a higher energy and entropy than molecular vapor. As a result, the original ANEOS underestimates vapor production for substances that form molecular species, including mantle rock. Melosh (2007) improved ANEOS to treat molecular vapor, considering one type of diatomic (or alternatively, triatomic) molecule as representative of a given material's vapor. This is a simplifying assumption, since vapor may in reality contain several different types of molecules with varying binding energies, but is a substantial improvement over the prior treatment of vapor as a mixture of pure monatomic species. Our SPH simulations consider dunite/forsterite mantles (with M-ANEOS parameters provided by E. Pierazzo and H.J. Melosh; e.g., Canup et al., 2002) and iron ANEOS cores, as in Canup (2004a, 2008). Our CTH simulations use both M-ANEOS for SiO₂ (with coefficients from Melosh, 2007) and M-ANEOS for dunite as representative mantle materials. CTH version 9.1 requires a slightly different set of M-ANEOS parameters for dunite than used in the SPH simulations (Canup et al., 2002; Canup, 2004a, 2008), and these are given in Appendix A.

3.4. Simulation analysis

We use an iterative procedure to determine whether material is in the planet, in bound orbit around the planet, or escaping (as in Canup et al., 2001; Canup, 2004a, 2008). An initial guess is made for the planet's size and therefore its mass (M_p) assuming a mean planet density comparable to that of the Earth. For each bound particle/cell that is outside the planet, we compute an equivalent circular orbit semi-major axis, a_{eq} , defined by setting $\sqrt{GM_p a_{eq}}$ equal to the particle/cell's specific angular momentum normal to the equatorial plane of the planet. The equivalent circular orbit is representative of that to which the mass represented by a particle or cell would settle after undergoing mutual collisions, which rapidly damp orbital eccentricities and inclinations but transport angular momentum much more slowly. Those particles/cells with a_{eq} greater than the equatorial radius of the planet are defined as being "in the disk", and those that are energetically unbound as escaping. The mass of the planet is then recomputed as the total mass minus the mass of the disk and the mass of escaping particles, and the process is repeated until convergence is achieved on M_p . Given the calculated disk mass, M_D , and angular momentum, L_D , we use Eq. (1) to estimate the mass of the Moon that could form from the disk, M_M . We make the favorable assumptions that $M_{esc} = 0$ and $\lambda = 1.3$.

We use the above procedure to compute M_D , L_D , and M_M at approximately 0.1–1 h intervals throughout each simulation. These quantities are strongly time-dependent for the first few to ten hours. In the immediate aftermath of a large, oblique impact, the portion of the impactor that grazes past the target forms a distorted, elongated structure. Gravitational torques both across this structure and between this structure and the distorted shape of the post-impact planet drive an increase in both the specific angular momentum of the "disk" and the calculated Moon mass (M_M),

with M_M typically achieving its maximum value in the ~ 2 –9 h period. Subsequent to this, the disk mass (M_D) generally decreases with time. Large clumps of material on highly eccentric orbits often remain after the initial impact, and some of these either re-impact the planet or pass deep within the Roche limit and are tidally disrupted, with either event causing a drop in M_D . As clumps with periapses well interior to the Roche limit are removed and/or destroyed, the disk quantities become more constant with time.

The disk properties also evolve due to numerical effects associated with the SPH and CTH methods. In SPH, M_D progressively decreases due to the artificial viscosity associated with the large smoothing lengths of the disk particles. SPH implements an artificial viscosity for treating shocks, with terms that vary linearly and quadratically with the velocity divergence in regions where the flow is converging (e.g., Balsara, 1995). The linear term has been shown to produce an effective kinematic shear viscosity $\nu \sim \bar{\alpha} ch/8$, where $\bar{\alpha} \sim$ unity is the code's linear viscosity parameter, c is the sound speed, and h is the characteristic particle smoothing length (Murray, 1996). For disks produced in $N = 10^6$ [$N = 10^5$] SPH simulations (e.g., Section 4.2), the mean smoothing length in the disk is typically $\langle h \rangle \sim 10^3$ to few $\times 10^3$ km [$\langle h \rangle \sim$ few $\times 10^3$ – 10^4 km], with $\langle c \rangle \sim 1$ –3 km s⁻¹. The spreading timescale of a disk of radial extent r is $t_\nu \sim r^2/\nu$, with $t_\nu \sim 10^2$ to few $\times 10^2$ h predicted for the disks produced in the $N = 10^5$ – 10^6 -particle SPH runs. In contrast, proposed physical sources of viscosity in the protolunar disk would spread the disk in ~ 0.1 to 10^2 years (Ward and Cameron, 1978; Thompson and Stevenson, 1988). Thus the SPH code's viscosity drives an artificially rapid spreading of the disk. Because material spreading onto the Earth typically has low angular momentum, it fractionally removes more mass than angular momentum from the disk, so that numerical spreading causes an artificially rapid decrease in M_D with time, but leads to an artificial increase in the disk's specific angular momentum, $J_D \equiv L_D/M_D$, with time (shown in our plots as the scaled quantity j_{disk}). In Appendix B, we estimate that in the course of a ~ 25 –50 h simulation with $N = 10^5$ – 10^6 particles, numerical spreading artificially decreases the disk mass by up to $\sim 10\%$ and increases the disk's specific angular momentum by a few percent. The predicted mass of the Moon (M_M) given by Eq. (1) is not appreciably affected by numerical spreading. A similar effect may be seen in CTH, which has similar artificial viscosity terms. However, the linear term is an order of magnitude smaller than in SPH. Being an Eulerian method CTH will have dissipation due to advection which can contribute an unknown amount to disk dissipation. This will be investigated in future work.

In SPH, all particles are retained throughout the simulation, so that the total mass is conserved absolutely and the fractional change in the total angular momentum is typically $\sim 10^{-5}$ – 10^{-4} . However in CTH, material can potentially flow outside the simulation grid and its mass and angular momentum are then lost. The total width of our smallest grid is $125R_\oplus$, and the maximum individual cubical cell width, used in the lowest density regions including typically those along the grid's outer boundaries, is $\sim 30R_\oplus$. Disk material at distances larger than $\approx 30R_\oplus$ from the origin (located at the center of the grid) can then fall within a cell along the grid's boundary and potentially advect out of the grid. It takes a particle leaving the Earth's surface at the escape velocity about 20 h to reach a distance $r = 30R_\oplus$; thus for $t < 20$ h, material leaving the grid will be on escaping trajectories and will not affect the calculated properties of the disk. For $t > 20$ h, it is possible for material leaving the grid to include material on highly eccentric bound orbits. Because this material would fractionally remove more angular momentum than mass, its loss would cause an artificial decrease in both the disk's specific angular momentum and the predicted Moon mass, M_M , with time. Mass loss from the grid is less than $\sim 0.15M_L$ in all of the cases shown here and so has a relatively minor influence on the outcomes of the CTH simulations.

Table 1
Effects of resolution and simulation method on results of impact simulations.

Run	γ	M_T/M_\oplus	b'	v_{imp}/v_{esc}	Smallest zone width (km)	Method	Final M_D/M_L	Final L_D/L_{EM}	Final L_F/L_{EM}	Final M_M/M_L	Disk iron fraction	Disk impactor fraction
<i>Resolution</i>												
amr1	0.11	1.02	0.82	1.0	781	CTH	0.61	0.10	1.10	0.35	10^{-7}	0.81
amr2	0.11	1.02	0.82	1.0	391	CTH	0.86	0.13	1.07	0.34	10^{-4}	0.87
amr3	0.11	1.02	0.82	1.0	195	CTH	0.57	0.09	0.97	0.25	0.20	0.71
amr4	0.11	1.02	0.82	1.0	98	CTH	0.89	0.14	0.99	0.45	0.03	0.73
Run 119	0.13	1.02	0.72	1.0	567 ^a	SPH	1.46	0.33	1.24	1.50	0.01	0.88
Run 119	0.13	1.02	0.72	1.0	263 ^a	SPH	1.32	0.27	1.14	1.30	0.08	0.80
Run 119	0.13	1.02	0.72	1.0	122 ^a	SPH	1.69	0.33	1.16	1.60	0.07	0.76
Run 16b ^b	0.13	1.02	0.72	1.0	263 ^a	SPH	1.93	0.35	1.21	1.56	0.03	0.81
Run 16b ^b	0.13	1.02	0.72	1.0	122 ^a	SPH	2.02	0.36	1.19	1.62	0.03	0.73
Run 87 ^c	0.20	1.02	0.75	1.0	312 ^a	SPH	2.00	0.39	1.10	1.94	0.09	0.62
Run 87 ^c	0.20	1.02	0.75	1.0	122 ^a	SPH	1.89	0.35	1.09	1.67	0.05	0.62
Run 83 ^d	0.20	1.02	0.65	1.0	312 ^a	SPH	1.57	0.30	1.13	1.40	0.05	0.70
Run 83 ^d	0.20	1.02	0.65	1.0	122 ^a	SPH	1.54	0.26	1.14	1.00	0.07	0.55
<i>Method</i>												
Run 119	0.13	1.02	0.72	1.0	197	CTH	1.32	0.27	1.15	1.32	0.03	0.85
Run 119	0.13	1.02	0.72	1.0	263 ^a	SPH	1.32	0.27	1.14	1.30	0.08	0.80
Run 119	0.13	1.02	0.72	1.0	122 ^a	SPH	1.69	0.33	1.16	1.60	0.07	0.76
Run 121	0.13	1.02	0.72	1.05	197	CTH	0.88	0.20	1.07	0.88	0.10	0.81
Run 121	0.13	1.02	0.72	1.05	263 ^a	SPH	1.65 ^e	0.31 ^e	1.15	1.50 ^e	0.08	0.79
Run 121	0.13	1.02	0.72	1.05	122 ^a	SPH	1.07	0.22	1.07	1.07	0.11	0.81
Reufer	0.20	1.04	0.50	1.3	197	CTH	1.01	0.15	1.22	0.47	0.05	0.33
Reufer	0.20	1.04	0.50	1.3	182 ^a	SPH	1.22	0.18	1.22	0.58	0.07	0.45

^a The 10^4 , 6×10^4 , 10^5 , 3×10^5 and 10^6 particle SPH simulations have individual particle masses of 6×10^{23} , 10^{23} , 6×10^{22} , 2×10^{22} , and 6×10^{21} g, respectively. Converting these masses into equivalent cubical cell widths assuming a density of 3.3 g cm^{-3} gives 566, 312, 263, 182, and 122 km, respectively.

^b Run 16b has a prograde pre-impact spin in the target with a 116 h rotation period.

^c Run 87 has a retrograde pre-impact spin in the target with a 4.1 h rotation period.

^d Run 83 has a retrograde pre-impact spin in the target with a 6.3 h rotation period.

^e SPH run 121 with $N = 10^6$ particles has a large intact clump that will pass well within the Roche limit on a timescale longer than can be simulated. This event would be expected to reduce M_D , L_D , and M_M .

4. Results

4.1. Resolution effects

4.1.1. Oblique, low-velocity collision with CTH

We begin by comparing results obtained by using AMR-CTH to simulate a giant impact at four resolutions with an impactor-to-total mass ratio $\gamma = 0.11$, a total colliding mass $M_T \sim 1.02M_\oplus$, a scaled impact parameter $b' = 0.82$, and an impact velocity $v_{imp} = v_{esc}$, where $v_{esc} = \sqrt{2GM_T/(R_i + R_t)}$, and R_i and R_t are the radii of the impactor and target. This is similar to run #24 from Canup and Asphaug (2001). That work considered a basalt mantle and the Tiltotson equation of state, which leads to a more massive disk compared to the same impact modeled with a silicate mantle described by ANEOS (Canup, 2004a). The CTH simulations in this section have SiO_2 mantles for the impactor and target described by M-ANEOS using the coefficients provided in Melosh (2007).

Fig. 2 shows results at two resolutions. The higher resolution case (with a minimum cell width of 98 km) required 6 days on 256 processors to simulate 48 h of evolution post-impact. Fig. 3 shows the time-evolution of several properties of the system as a function of numerical resolution: the disk mass, the disk specific angular momentum, and the predicted Moon mass from Eq. (1). Several trends are apparent from Figs. 2 and 3. First, it takes between 20 and 30 h for quantities such as the orbiting disk mass to settle to relatively constant values. Prior to this time, there are frequent re-impacts of large clumps of ejected material with the planet, which change each of these calculated quantities. Second, the time to achieve steady state generally increases as zone size decreases. Coarser numerical resolution leads to greater artificial viscosity, which drives more rapid radial spreading of orbiting material. With lower resolutions, this effect causes clumps to re-impact the planet sooner, so that the plotted quantities stabilize

sooner as well. The final disk mass and angular momentum are broadly similar across all four runs, with $\langle M_D/M_L \rangle = 0.73 \pm 0.14$ and $\langle L_D/L_{EM} \rangle = 0.12 \pm 0.02$, but the predicted iron mass fraction in the disk varies greatly, from $\sim 10^{-2}$ to 10^{-1} for the two higher resolution runs to $\leq 10^{-4}$ in the two low resolution runs. The total mass in orbiting iron is not well resolved by the lower resolution simulations. In addition, the amount of iron in the final disk is sensitive to the angle at which the large clump containing the impactor core re-collides with the Earth, and this varies from case to case. The mass fraction of the disk originating from the impactor is similar across the four runs, with an average value of 0.78 ± 0.06 .

4.1.2. Oblique, low-velocity collision with SPH

Next we simulate a collision using SPH with $N = 10^4$, 10^5 , and 10^6 particles, corresponding to individual particle masses of approximately 6×10^{23} , 6×10^{22} and 6×10^{21} g, respectively, implying an equivalent cubical cell width of about 567 km, 263 km, and 122 km for mantle material at the reference density of $\rho = 3.3 \text{ g cm}^{-3}$. The factor of 10^2 variation in individual particle mass corresponds to a difference of $(10^2)^{1/3} \sim 5$ in linear resolution across the three runs for a fixed density. We consider a potential Moon-forming impact comparable to run 119 shown in Fig. 2 of Canup (2004a): $\gamma = 0.13$, a total mass $M_T \approx 1.02M_\oplus$, $b' = 0.72$, $v_{imp} = v_{esc}$, and $L_{col} \approx 1.25L_{EM}$. We use M-ANEOS for dunite for the target and impactor mantles in our SPH simulations, as in Canup (2004a, 2008).

Fig. 4 shows comparative time sequences from the three runs. In the hour following an oblique, low-velocity (i.e., $(v_{imp}/v_{esc}) \sim 1$) collision, the impactor material that has grazed past the target initially forms an elongated structure that is nearly in line with its original trajectory. As this material undergoes Keplerian motion, its inner portions rotate ahead of the outer portions, producing a structure coarsely resembling a trailing spiral arm. Gravitational

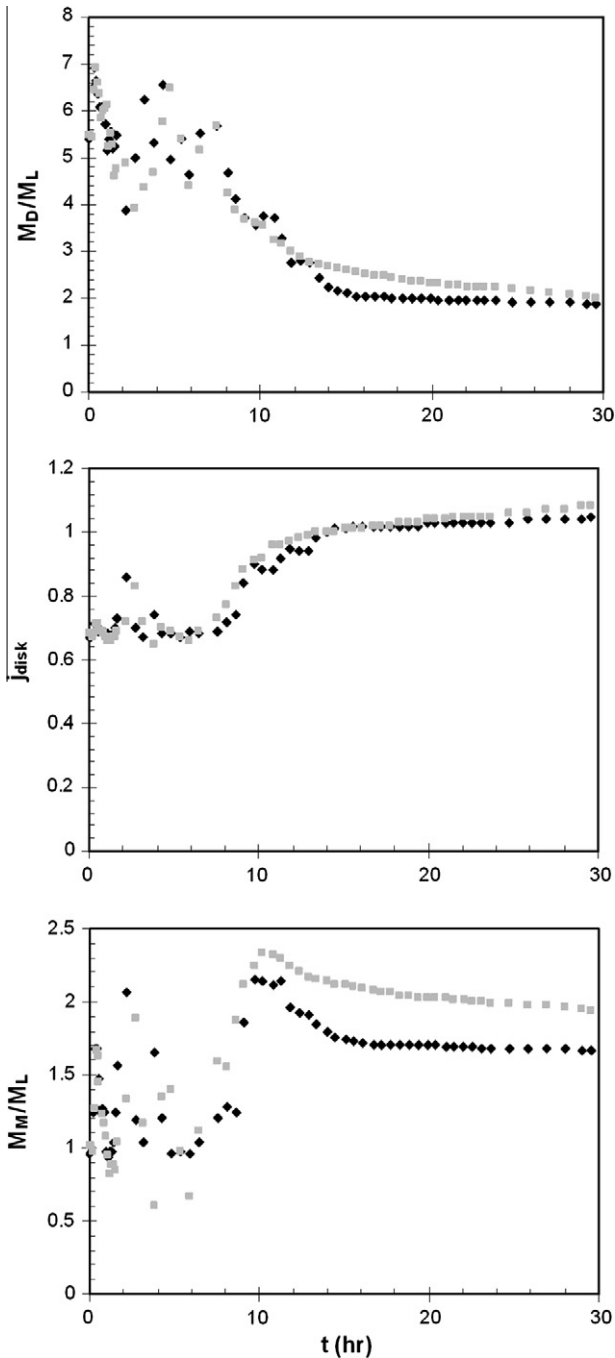


Fig. 8. SPH simulations of an impact into a rapidly retrograde rotating target by a $\gamma = 0.2$ impactor. Results shown for two resolutions ($N = 6 \times 10^4$, gray squares; $N = 10^6$, black diamonds).

torques across this structure allow its outer portions to gain angular momentum and achieve orbit at the expense of inner portions, which re-collide with the Earth. The inner portions of the arm (that consist primarily of the impactor's iron core) re-coalesce into a large clump that re-impacts the planet (see Fig. 4 and 3.8 h), removing the most of the impactor's iron from orbit.

Fig. 5 shows the time-evolution of disk properties from the Fig. 4 simulations. All three SPH resolutions produce similar results for the first few hours of the simulation, suggesting that the primary impact event and the immediate post-impact partitioning of energy and angular momentum are well-resolved for $N > 10^4$. With time the dynamics of the system becomes increasingly con-

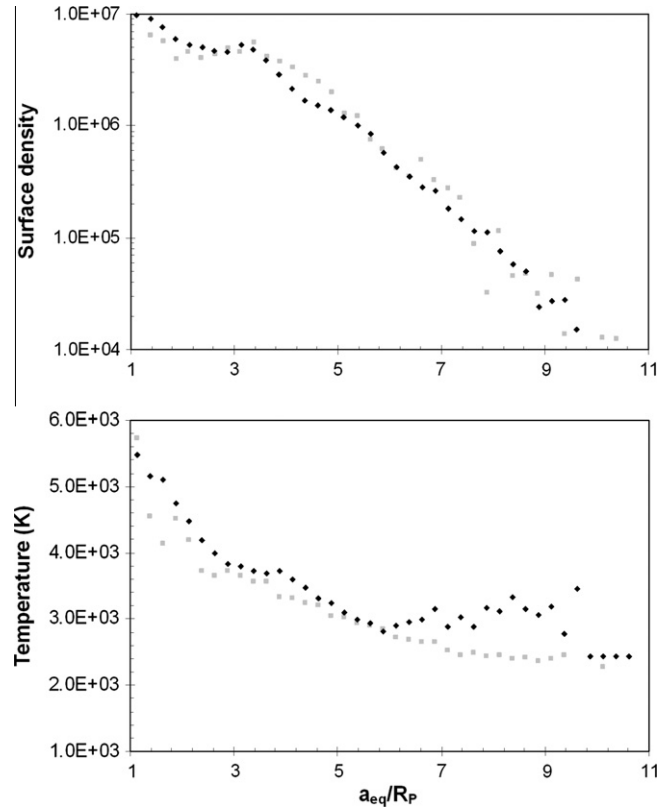


Fig. 9. Surface density (g cm^{-2} ; top) and temperature (bottom) vs. equivalent circular orbit in units of the planet's radius for the $N = 10^6$ (filled diamonds) and 6×10^4 (gray squares) particle SPH simulations shown in Fig. 8.

trolled by the specific masses and orbits of large clumps, and is therefore sensitive to individual conditions that vary across the simulations. As the inner clump containing the bulk of the impactor's core re-collides with the planet, an abrupt drop in orbiting mass occurs at $t \sim 6$ h for the two higher resolution runs, and at $t \sim 4.5$ h for the lowest resolution run, in which the iron-containing clump is less coherent (Fig. 5b). After this iron-removing collision, the subsequent evolution differs in each case. In the $N = 10^4$ particle run, an additional exterior intact clump containing $1.1M_L$ of pure dunite remains on an ultimately stable orbit with $a = 4.5R_\oplus$, $e = 0.23$ and a periape well outside the Roche limit at $3.4R_\oplus$. Thus the low-resolution run produces an intact iron-free Moon containing most of the orbiting mass. In the $N = 10^5$ run, the exterior clump re-impacts the Earth in a grazing collision at about 19 h, and is tidally disrupted and dispersed. The final disk in this case contains some small clumps, the largest of which contain a few percent of a lunar mass. The mid-resolution run thus produces a disk without a large intact Moon. The million-particle simulation has two large exterior clumps, one of which collides with the Earth at about 40 h and the other of which is left in a stable orbit with $a \sim 4R_\oplus$, and a periape at approximately the Roche limit, so that the end result in this case is a disperse disk containing $\sim 0.9M_L$ together with an intact Moon (mass $0.75M_L$) that undergoes substantial tidal distortion during each periape passage.

SPH as a method is known to be capable of producing spurious clumping and, in particular, small-scale filamentary structures in simulations of shear flows (e.g., Nelson et al., 1998; Imaeda and Inutsuka, 2002). However clumps represented by a great multitude of SPH particles (as is the case for the larger clumps in the $N = 10^5$ and $N = 10^6$ particle runs) are likely to be physically realistic. The surface density of the elongated structure of impactor material between the $t = 1$ h and the $t = 3.8$ h frames of the SPH simulations is

high-enough to expect the formation of lunar-mass and larger clumps due to gravitational instability (e.g., Goldreich and Ward, 1973). In addition, similar scale clumps are seen in the CTH simulation (see Section 4.2.1).

Differences in clump formation and evolution lead to substantial differences in the predicted disk mass and angular momentum in the 10–40 h time period (Fig. 5). However by 50 h the last of the large clumps with a periape interior to the Roche limit has completed at least one orbit, and the predictions of all three runs converge more closely, with an average final disk mass $\langle M_D/M_L \rangle = 1.49 \pm 0.15$ and disk angular momentum $\langle L_D/L_{EM} \rangle = 0.31 \pm 0.03$. The 10^6 (10^5) [10^4] particle run has a final disk mass at $t = 50$ h of $1.69M_L$ ($1.32M_L$) [$1.46M_L$], a disk angular momentum $0.33L_{EM}$ ($0.27L_{EM}$) [$0.33L_{EM}$], a bound system angular momentum $L_F = 1.16L_{EM}$ ($1.14L_{EM}$) [$1.24L_{EM}$], a disk iron fraction 0.07 (0.08) [0.005], a disk impactor fraction 0.76 (0.80) [0.88], and a predicted final Moon mass of $1.6M_L$ ($1.3M_L$) [$1.5M_L$]. Of the orbiting particles, 39% (56%) [82%] have orbital periapees outside the Roche limit, while 63% (71%) [92%] have equivalent circular orbits exterior to a_R . The trend in these two variables with resolution reflects an increase in the final disk specific angular momentum as resolution is decreased, with $j_{disk} = 1.09$, 1.15, and 1.24 for $N = 10^6$, 10^5 , and 10^4 , respectively. This is consistent with the increasing effects of numerical spreading as resolution decreases (Appendix B). Fig. 6a–b show the radial surface density and average temperature profiles at $t = 50$ h, where we have binned orbiting particles by their equivalent circular orbit semi-major axis, a_{eq} . In the $N = 10^6$ (10^5) [10^4] particle run, 90% of the disk mass has $a_{eq} < 5.5R_p$ ($a_{eq} < 6R_p$) [$a_{eq} < 7R_p$], where R_p is the radius of the post-impact planet. The single large intact Moon in the $N = 10^4$ particle simulation is reflected in the surface density peak near $a_{eq} \sim 4R_p$. Fig. 6c shows the evolution of the disk’s vapor fraction, which is less than 25% over the time period when the disk is established; these values are comparable to those computed for similar collisions and total simulation times in Canup (2004a).

Overall the three simulations converge very closely in the early stages of the impact and post-impact, diverge considerably in the mid-stages as the chaotic dynamics of individual clumps affects calculated disk quantities, and converge relatively closely once the system has been tracked long enough for clumps on orbits that will pass within the Roche limit to have done so. It appears probable that the final convergence is physically based and is not caused by numerically induced spreading, because the latter causes the disk mass and angular momentum of simulations at varied resolutions to diverge rather than converge with time (Appendix B and Fig. B1). Similar to the CTH resolution study above, we find that as numerical resolution is increased, the time required for the disk properties to stabilize increases as well, due to a later characteristic time for large clump disruptions/re-impact with the planet as resolution is increased. The formation of a large intact Moon is a sensitive function of the orbital elements of the largest clump(s), with both disperse disk and intact Moon cases obtained here from the same collision at different resolutions.

4.1.3. SPH: Slow pre-impact prograde target

We next use SPH to simulate the same collision as in Section 4.1.2, but with a slow, 116-h rotational day in the target prior to the collision. The spin axis of the pre-impact target is aligned with the collisional angular momentum, so that it is a “prograde” pre-impact spin as defined in Canup (2008); this collision is analogous to run 16b in that paper and has $L_{col} \approx 1.26L_{EM}$. Fig. 7 shows the evolution of the disk properties for two resolutions (10^5 and 10^6 particles). The results of these simulations are similar across the entire run time. At the end of the simulations, both cases are left with a single large exterior clump on an extremely eccentric orbit that will ultimately pass well within the Roche limit and be

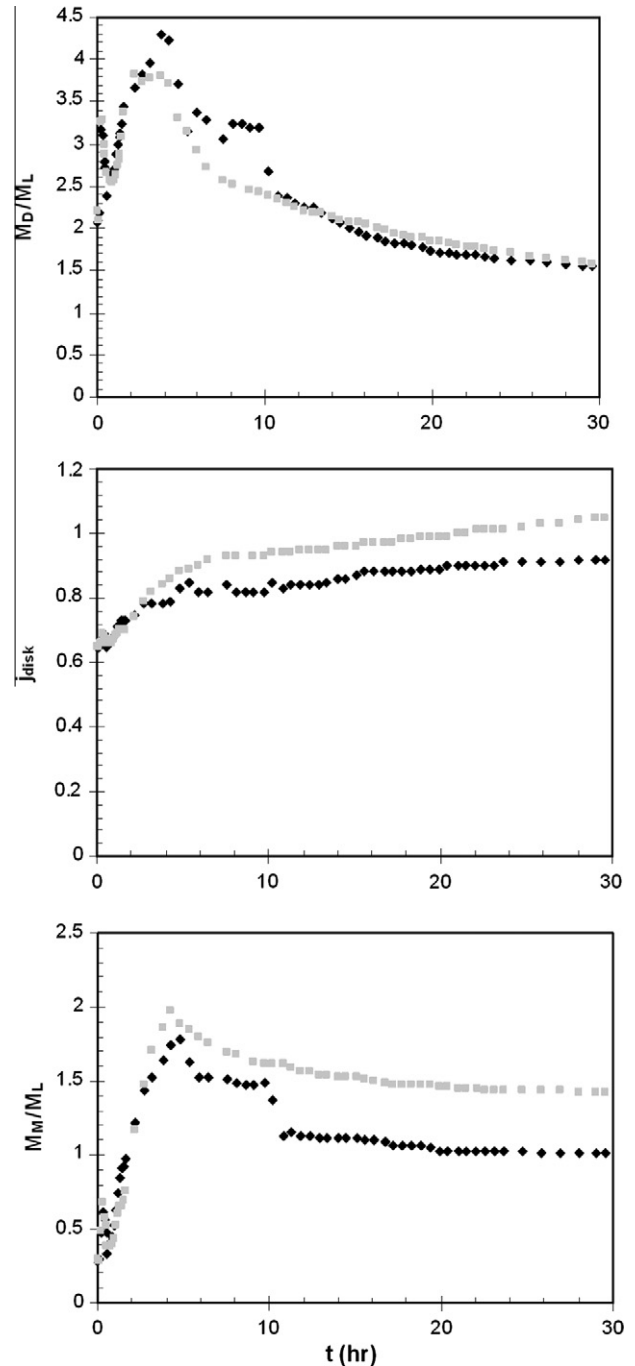


Fig. 10. SPH simulations of an impact into a rapidly retrograde rotating target by a $\gamma = 0.2$ impactor with a somewhat less oblique impact than the Fig. 9 case. Results shown for two resolutions ($N = 6 \times 10^4$, gray squares; $N = 10^6$, black diamonds).

disrupted, with this event occurring on a timescale longer than is simulated here. The 10^6 (10^5) particle final clump is 100% (100%) dunite, contains $1.01M_L$ ($0.784M_L$), and has an orbit with $a = 14R_{\oplus}$ ($a = 8.8R_{\oplus}$), $e = 0.92$ ($e = 0.86$), and a periape of $1.2R_{\oplus}$ ($1.2R_{\oplus}$). The 10^6 (10^5) particle run has a final disk mass at $t = 35$ h of $2.02M_L$ ($1.93M_L$), disk angular momentum $0.36L_{EM}$ ($0.35L_{EM}$), bound system angular momentum $1.19L_{EM}$ ($1.21L_{EM}$), disk iron fraction 0.05 (0.03), disk impactor fraction 0.73 (0.81), and a predicted final Moon mass of $1.62M_L$ ($1.56M_L$). Of the orbiting particles, 20% (29%) have orbital periapees outside the Roche limit.

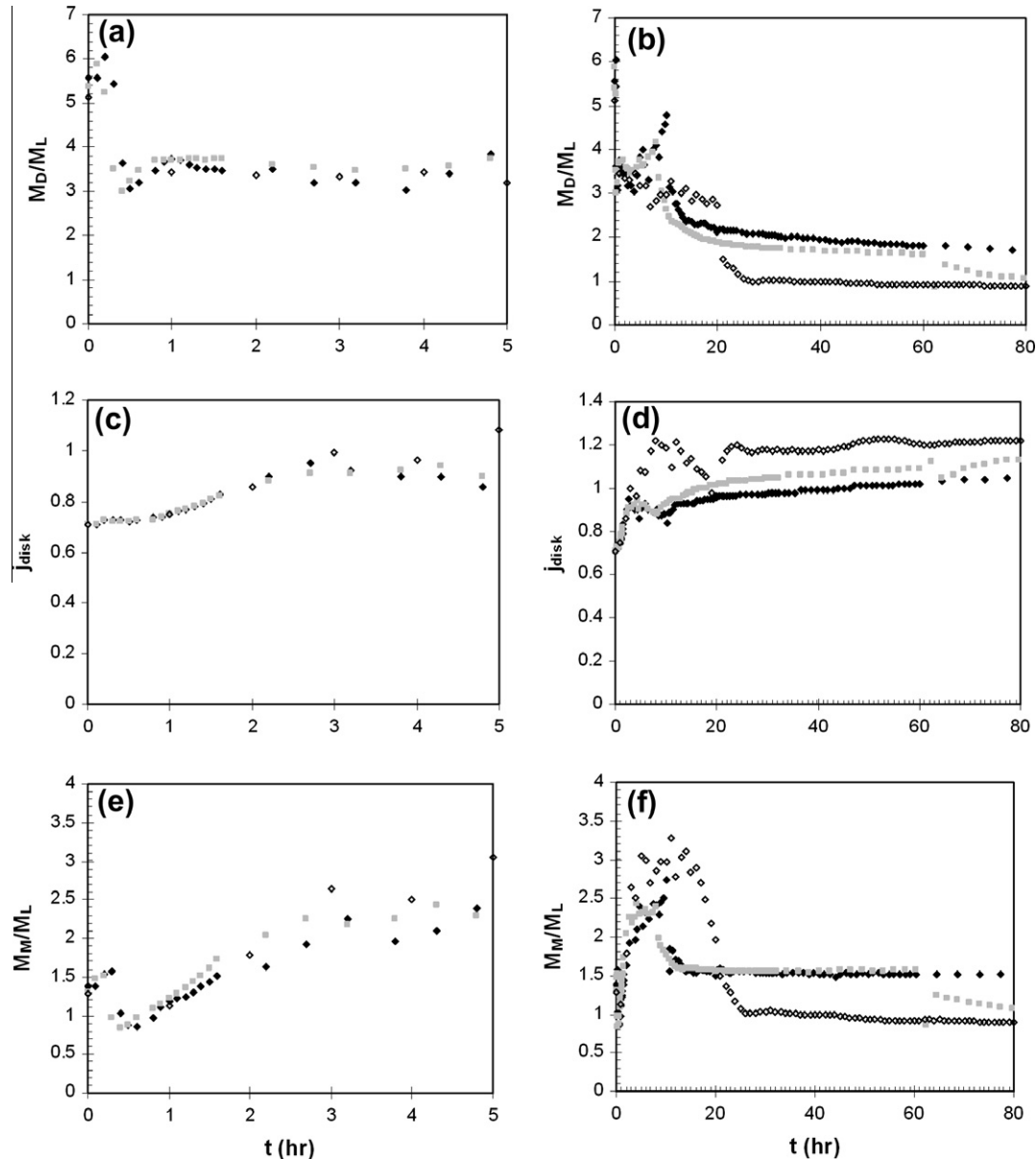


Fig. 11. Same collision and quantities as in Fig. 5, only here with $v_{imp} = 1.05v_{esc}$. SPH simulation results shown for two resolutions ($N = 10^5$, gray squares; $N = 10^6$, black solid diamonds), and CTH results (open diamonds).

4.1.4. SPH: Larger impactor and retrograde pre-impact spin in target

A rapid retrograde spin in the protoearth before the Moon-forming collision (i.e., a pre-impact spin in the opposite sense of the impact itself) allows for a more massive impactor while still satisfying $L_{col} \approx L_{EM}$. We use SPH simulate a collision comparable to run 87 in Canup (2008, Table 1), which has $\gamma = 0.20$, a total mass $M_T \approx 1.02M_{\oplus}$, $b' = 0.75$, $v_{imp} = v_{esc}$, a retrograde, 4.1 h pre-impact rotational period in the target, and $L_{col} \approx 1.18L_{EM}$. Relatively close convergence of disk properties is seen for the $N = 6 \times 10^4$ and $N = 10^6$ runs across the entire simulation (Fig. 8). At $t = 30$ h, the 10^6 (6×10^4) particle run has a final disk mass of $1.89M_L$ ($2.00M_L$), disk angular momentum $0.35L_{EM}$ ($0.39L_{EM}$), bound system angular momentum $1.10L_{EM}$ ($1.09L_{EM}$), disk iron fraction 0.05 (0.09), disk impactor fraction 0.62 (0.62), and a predicted final Moon mass of $1.67M_L$ ($1.94M_L$). Of the orbiting particles, 35% (57%) have orbital periaapses outside the Roche limit. Both cases produce an orbiting disk with only small clumps ($\sim 1\%$ of a lunar

mass or smaller). Fig. 9 shows the corresponding surface density and temperature distributions at $t = 30$ h for both simulations.

Fig. 10 shows a similar collision with a somewhat less oblique impact, with $\gamma = 0.20$, a total mass $M_T \approx 1.02M_{\oplus}$, $b' = 0.65$, $v_{imp} = v_{esc}$, a 6.3 h pre-impact retrograde rotational period in the target, and $L_{col} \approx 1.19L_{EM}$ (comparable to run 83 in Canup, 2008). In both the $N = 6 \times 10^4$ and $N = 10^6$ runs, two large clumps form after the initial impact, with the innermost clumps colliding with the planet at ~ 4 –5 h and the outermost clumps colliding with the planet after ~ 7 –10 h. Both cases ultimately produce a disk with only small clumps containing $< 0.01M_L$ each. The 10^6 (6×10^4) particle run has a final disk mass at $t = 30$ h of $1.54M_L$ ($1.57M_L$), disk angular momentum $0.26L_{EM}$ ($0.30L_{EM}$), bound system angular momentum $1.14L_{EM}$ ($1.13L_{EM}$), disk iron fraction 0.07 (0.04), disk impactor fraction 0.55 (0.70), and a predicted final Moon mass of $1.0M_L$ ($1.4M_L$). Of the orbiting particles, 11% (43%) have orbital periaapses outside the Roche limit.

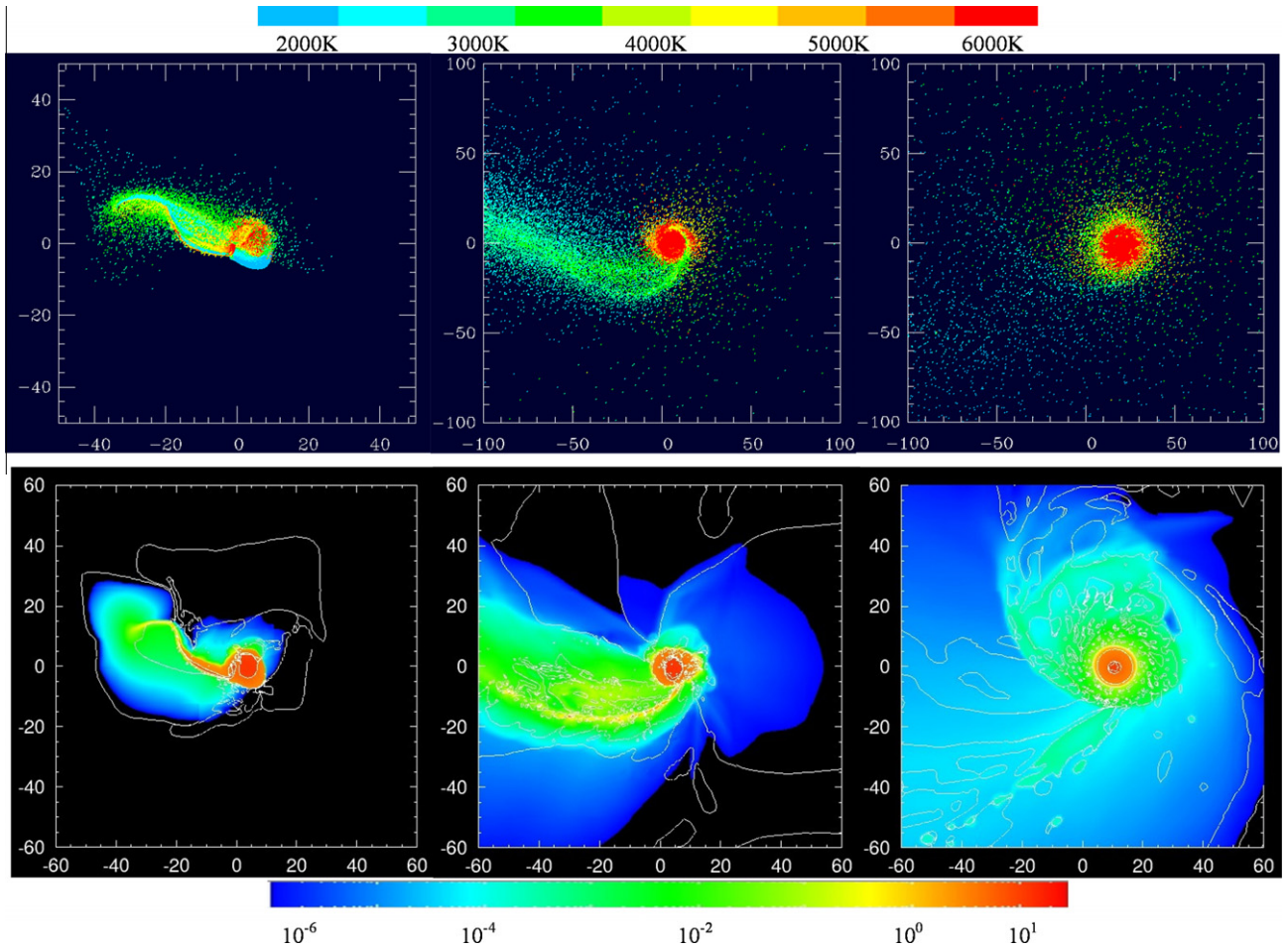


Fig. 12. SPH simulation (top) with $N = 3 \times 10^5$ of an impact with $\gamma = 0.2$, $v_{\text{imp}} = 1.3v_{\text{esc}}$, and $b' = 0.50$; this is the higher-velocity, more head-on collision advocated by Reufer et al. (2011). Distances shown in units of 10^3 km; color scales with temperature, per color bar, with data from all SPH particles overplotted. Results are shown at $t = 1.0$ h (top left), 5.3 h (top middle), and 23.5 h (top right). CTH simulation of the same impact (bottom) are shown at comparable times with color scaling as mid-plane density as indicated by the color bar (units in g cm^{-3}).

4.2. SPH vs. CTH

4.2.1. Oblique, low-velocity collision

Figs. 4 and 5 show results of the same collision described in Section 4.1.2 simulated with AMR-CTH. The CTH simulations here and in the next two sections use a domain $800,000$ km on a side (roughly $125R_{\oplus} \times 125R_{\oplus} \times 125R_{\oplus}$ in three dimensions) with a smallest cell width of 197 km, corresponding to a total mass per cubical cell $\sim 2.5 \times 10^{22}$ g for mantle material with $\rho = 3.3 \text{ g cm}^{-3}$, which is intermediate to the SPH particle masses in the $N = 10^5$ and 10^6 particle runs. We use the molecular ANEOS in CTH with parameters for dunite including molecular vapor (Appendix A) to describe the impactor and target mantles, which mimics that used in the SPH simulations. The CTH simulation here required 6 weeks on a 12 node dedicated cluster.

A similar sequence of events is seen in the CTH run as in the three SPH runs (Fig. 4, bottom row). After the initial impact, the impactor debris forms a massive, iron-rich inner clump together with a silicate-rich outer clump (3.8 and 5.4 h). The inner clump re-impacts the Earth (in this case at 9.6 h), causing a drop in the orbiting mass (Fig. 5a). The outer clump has a periapse that is somewhat interior to the Roche limit, and it is highly distorted and loses mass to tidal stripping as it passes through periapse at about 22 h and again at about 40 h (final frame in Fig. 4). At $t = 50$ h, the CTH disk iron and impactor fractions are 0.03 and 0.85, respectively; these quantities are similar to those from the

SPH runs. The CTH disk mass is $1.32M_L$, the disk angular momentum is $0.27L_{EM}$, and the predicted final Moon mass is $1.32M_L$. The final CTH disk mass at $t = 50$ h is 11% lower than the average disk mass of the three SPH runs, while the CTH disk angular momentum is about 13% lower than the corresponding average from the SPH runs. Of the orbiting particles, 43% have orbital periapses outside the Roche limit. The CTH final bound system angular momentum is $L_F = 1.15L_{EM}$, similar to the average obtained from the SPH runs. The final radial temperature and surface density distributions are also similar to those in the SPH runs, with 90% of the disk mass in the CTH simulation having $a_{\text{eq}} < 7R_P$. Mass loss from the grid is minimal during the simulation, $\sim 0.01M_L$.

4.2.2. Oblique collision with increased impact velocity

We next use SPH and CTH to simulate the same collision as in Sections 4.1.2 and 4.2.1, but here with a slightly higher impact velocity, $v_{\text{imp}} = 1.05v_{\text{esc}}$ and $L_{\text{col}} \approx 1.32L_{EM}$. Fig. 11 shows the evolution of the same quantities as in Fig. 5 for two SPH resolutions ($N = 10^5$ and 10^6) and a CTH simulation. Both SPH runs have a large, iron-rich clump re-impact the Earth between about 7 (low resolution run) and 10 (high resolution run) h. Both cases are then left with a large 100% dunite clump on a highly eccentric orbit with a periapse well inside the Roche limit. The clump in the $N = 10^5$ simulation passes through periapse at ~ 62 h and is tidally disrupted, leaving a dispersed disk. The final clump in the $N = 10^6$ particle contains $1.03M_L$ and has an orbit with $a = 101R_{\oplus}$, $e = 0.99$,

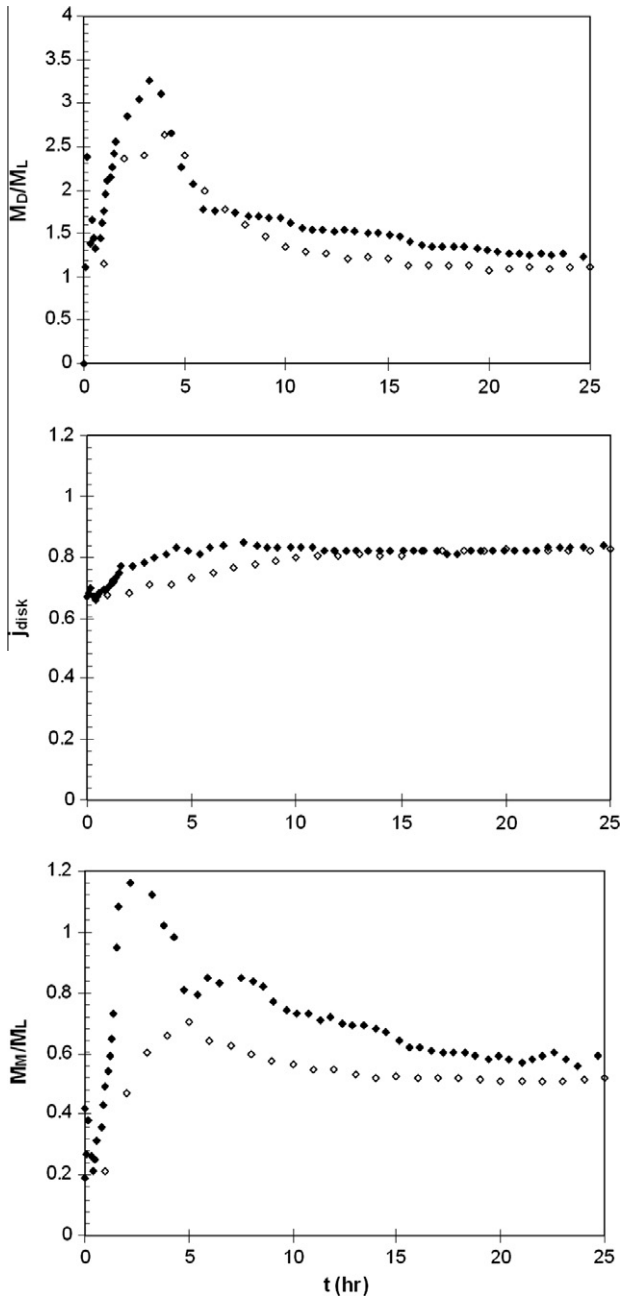


Fig. 13. Results of SPH simulation shown in Fig. 12 (black filled diamonds) compared with a CTH simulation of the same impact (open diamonds). Plots show the orbiting disk mass in lunar masses (top), the normalized angular momentum of the disk, j_{disk} , (middle), and the predicted mass of the resulting Moon (bottom).

and a periape of $1.45R_{\oplus}$, so that it will suffer a similar fate (although on a timescale longer than can be simulated here). The 10^6 (10^5) particle run has a final disk mass at $t \approx 80$ h of $1.65M_L$ ($1.07M_L$), disk angular momentum $0.31L_{EM}$ ($0.22L_{EM}$), bound system angular momentum $1.15L_{EM}$ ($1.11L_{EM}$), disk iron fraction 0.08 (0.11), disk impactor fraction 0.79 (0.81), and a predicted final Moon mass of $1.50M_L$ ($1.07M_L$). Of the orbiting particles, 24% (47%) have orbital periapees outside the Roche limit. The differences in disk mass and disk angular momentum between the two SPH runs is substantial due to the presence of the lunar-mass clump in the $N = 10^6$ particle run that has not yet completed a pass through its periape deep within the Roche limit.

Two large clumps also form in the CTH simulation in the first few hours following the initial impact. The inner clump re-collides

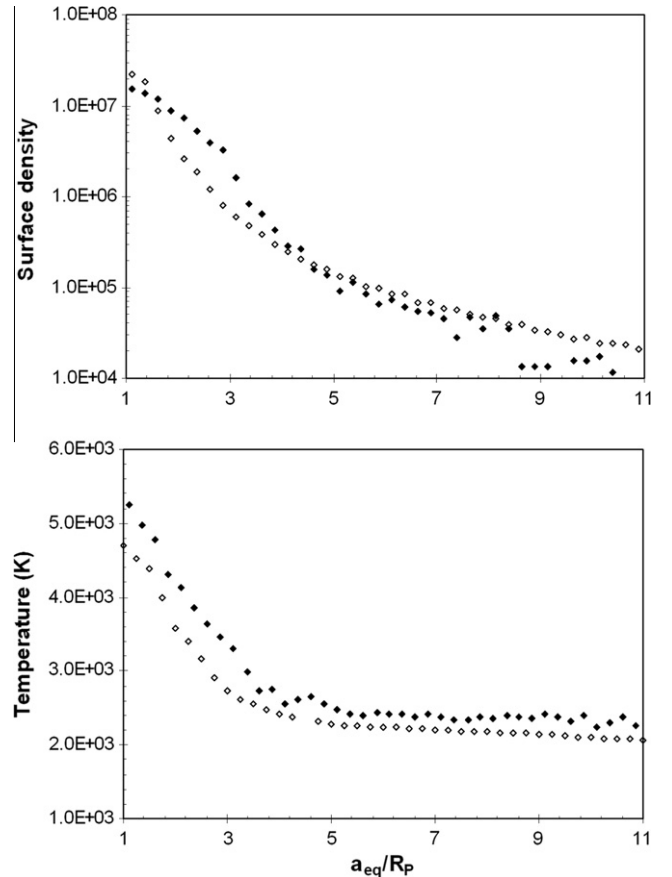


Fig. 14. Surface density (top; in g cm^{-2}) and temperature (bottom) vs. equivalent circular orbit in planetary radii for the final time step in the CTH (open diamonds) and SPH (filled diamonds) simulations shown in Figs. 12 and 13.

with the planet at $t \approx 20$ h, while the outer clump passes through its periape near the Roche limit at about 24 h and is highly tidally distorted but remains substantially intact. At $t = 80$ h, the CTH run has a final disk mass of $0.89M_L$, disk angular momentum $0.20L_{EM}$, bound system angular momentum $1.07L_{EM}$, disk iron fraction 0.10, disk impactor fraction 0.81, and a predicted final Moon mass of $0.88M_L$. Of the orbiting particles, 46% have orbital periapees outside the Roche limit. In both the CTH run and the 10^5 -particle SPH simulation, all large clumps with periapees well interior to the Roche limit have completed at least one orbit by $t = 80$ h. Comparing these two runs, the final CTH disk mass and angular momentum are 17% and 10% lower, respectively. We note that this CTH run is long enough that there is significant loss of mass ($\sim 0.14M_L$) due to material leaving the grid. This material leaves the grid at times $t > 40$ h, and so it may include bound disk material (see Section 3.4) and be partially or fully responsible for the decrease in the CTH calculated disk mass from $M_D = 0.99M_L$ at $t = 40$ h to $M_D = 0.89M_L$ at $t = 80$ h. Thus at least some of the difference between the CTH and SPH disk masses in this case is likely due to material leaving the CTH grid.

4.2.3. Less oblique, higher-velocity collision

Our final simulations consider a $\gamma = 0.2$, $v_{\text{imp}} = 1.3v_{\text{esc}}$, and $b' = 0.50$ collision as advocated in Reufer et al. (2011; see also Reufer et al., 2012). Here $L_{\text{col}} = 1.7L_{EM}$, and we use a slightly higher initial total mass ($M_T = 1.04M_{\oplus}$) to allow for an increased escaping mass compared to the low impact velocity simulations above. Fig. 12 shows frames from the CTH and the $N = 3 \times 10^5$ particle SPH simulations, while Fig. 13 compares results from both runs. Inner portions of the impactor material re-impact the planet in the 2–5 h time period,

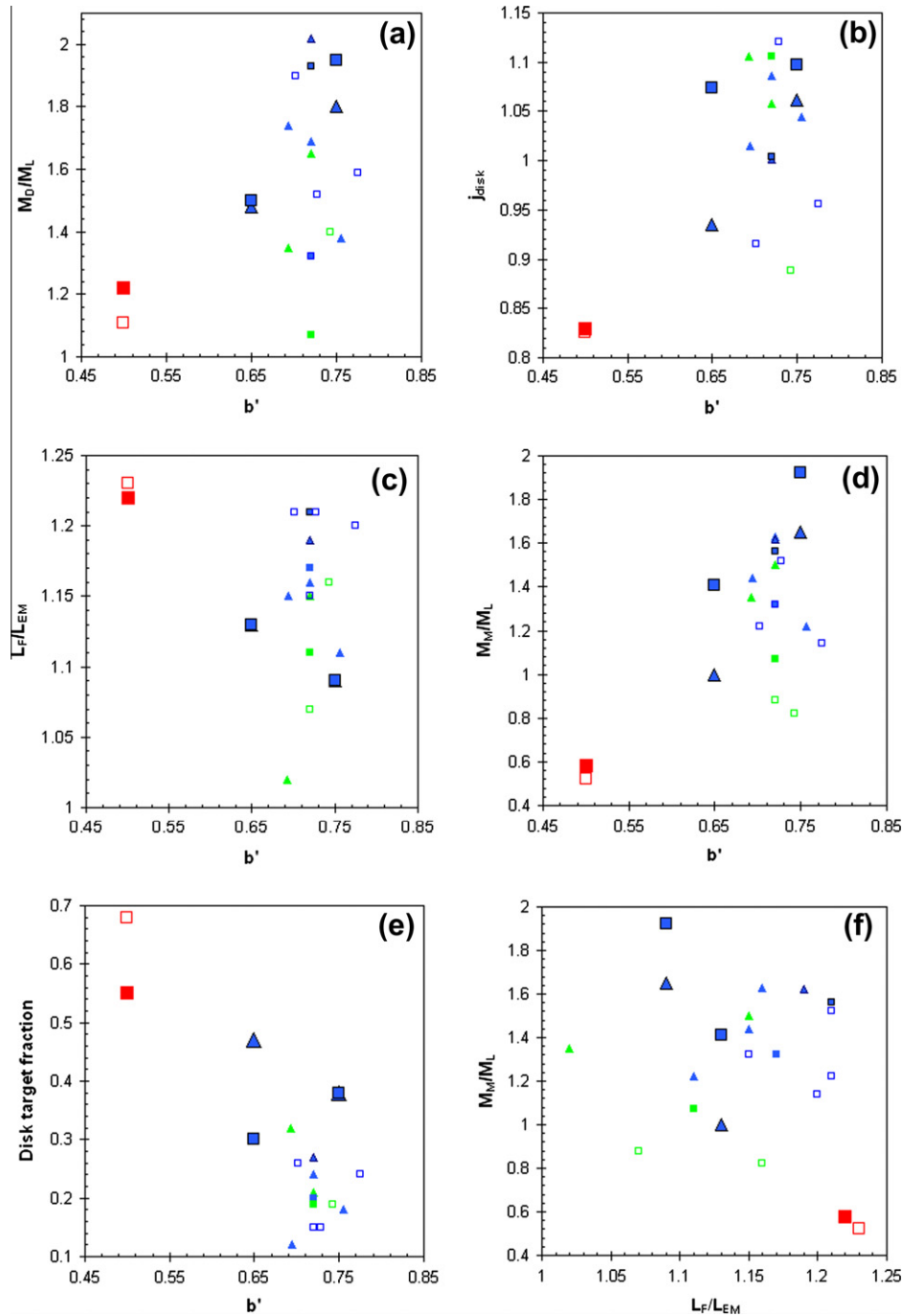


Fig. 15. Open squares are results of CTH simulations, while filled symbols are SPH results (with $N = 10^6$, triangles; $N \sim 10^5$, squares). Color indicates $v_{\text{imp}} = v_{\text{esc}}$ (blue), $v_{\text{imp}} = 1.05 v_{\text{esc}}$ (green), or $v_{\text{imp}} = 1.3 v_{\text{esc}}$ (red). Small symbols correspond to impacts with $\gamma = 0.13$, while large symbols correspond to $\gamma = 0.2$. SPH simulations involving pre-impact spin are indicated by symbols with black outlines. Plots show disk mass in lunar masses (a), normalized disk angular momentum (b), the post-impact system angular momentum (c), the predicted mass of the Moon that would later accrete from the disk (d), the fraction of the disk originating from the target Earth (e) and the predicted Moon mass vs. the final system angular momentum (f).

which reduces the disk mass (Fig. 13). At $t = 25$ h, the SPH (CTH) run has a disk mass of $1.22M_L$ ($1.11M_L$), disk angular momentum $0.18L_{EM}$ ($0.16L_{EM}$), bound system angular momentum $L_F = 1.22L_{EM}$ ($1.23L_{EM}$), disk iron fraction 0.07 (0.04), disk impactor fraction 0.45 (0.32), and a predicted final Moon mass of $0.58M_L$ ($0.52M_L$). Of the orbiting particles, 10% (11%) have orbital periaapses outside the Roche limit. Both simulations produce an orbiting disk with only small clumps ($\sim 1\%$ of a lunar mass or smaller). The CTH run predicts a disk mass and angular momentum that are each about 10% lower than the respective values from the SPH simulation. At $t = 25$ h, a mass of $0.16M_L$ has left

the grid in the CTH simulation. However because of the relatively short duration of this simulation, the great majority of this material would have been on escaping rather than bound orbits, and so should not have substantially affected the M_D , L_D and L_F values calculated for the CTH run. Fig. 14 shows the final radial surface density and temperature distributions for these two simulations. Both our SPH and CTH results are broadly similar to those provided for this run (their cc01) in Reufer et al. (2012), who report $M_D = 1.06M_L$, $L_F = 1.2L_{EM}$, a disk with an impactor mass fraction of 0.43, and a final predicted Moon mass of $0.52M_L$.

Table A1

Dunite M-ANEOS for CTH 9.1. This EOS closely matches that used in SPH simulations by Canup (2004a,b, 2008). It does not include rotational or vibrational terms in the free energy. It is implemented in CTH 9.1 as DUNITE_MOL.

Number	Value	description
V1	3	Nel; number of elements in material (Mg, Si, O)
V2	4	EOS; EoS Type; solid-gas with electronic terms and detailed treatment of liquid/vapor region
V3	3.32 g cm ⁻³	r_0 ; reference density
V4	0 eV	Reference temperature, defaults to 298 K.
V5	0	p_0 , reference pressure
V6	-6.6e5 cm s ⁻¹	S_0 , from shock-particle velocity relation, $u_s = S_0 + S_1 u_p$ Negative sign required
V7	0.82	G_0 , reference Gruneisen coefficient
V8	0.057 eV	Reference Debye temperature
V9	0.86	S_1 from linear shock-particle velocity relation, $u_s = S_0 + S_1 u_p$
V10	2	Three times the limiting value of G at large compressions ($3 * C24$)
V11	1.3e11 erg g ⁻¹	E_{sep} , Zero-T separation energy
V12	0.19 eV	melting temperature
V13	1.97e11	Parameter $c_{5,3}$, for low density modification to move the critical point
V14	0.8	Parameter $c_{5,4}$, for low density modification to move the critical point
V15	0	H_0 , thermal conductivity parameter; 0 if not included
V16	0	$c_{4,1}$, thermal conductivity parameter; 0 if not included
V17	0	Lowest allowed solid density – should default to 0.9 r_0
V18	4.65 g cm ⁻³	D1, Density at onset of high pressure phase transition (hppt)
V19	4.9 g cm ⁻³	D2, Density at completion of hppt
V20	6.6e11 dyne cm ⁻²	Pressure at center of hppt
V21	3.5e12 dyne cm ⁻²	dP/dh at end of hppt
V22	1.3e13 dyne cm ⁻²	d^2P/dh^2
V23	0	H_{fus} , heat of fusion
V24	0	Density of liquid at the melting point; negative sign flags ANEOS
V25..32	0	Not used in this EOS type
V33	1	Flag for ionization model. 0 = Saha; 1 = Thomas-Fermi
V34	0	E_{shift} , shift energy for reactive chemistry modeling
V35	0	S_{shift} , shift entropy for reactive chemistry modeling
V36 ^m	2	Number of atoms in molecular clusters
V37 ^m	8.0 eV	E_{bind}
V38 ^m	0	Rotational degrees of freedom
V39 ^m	0	R_{bond} , length of molecular bond
V40 ^m	0	Vibrational degrees of freedom
V41 ^m	0	Vibrational debye temperature
V42 ^m	1	Flags use of Lennard-Jones (in this case, Mie) potential
V43 ^m	1.27	Power in Mie potential
V44–48	0	Not used
Z	f	
8	0.571	
12	0.286	
14	0.143	

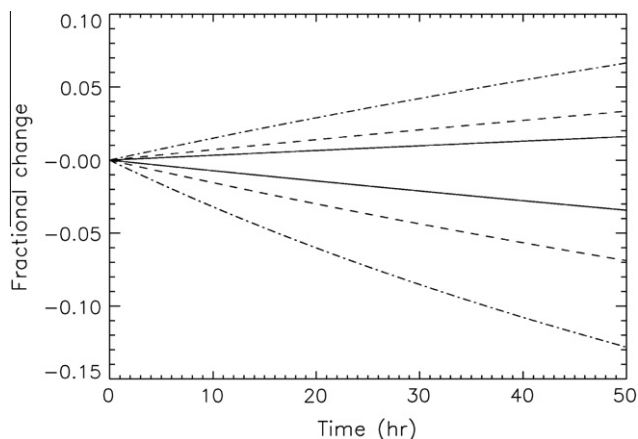


Fig. B1. Fractional decrease in the protolunar disk mass and increase in the disk specific angular momentum expected in 10^6 (solid), 10^5 (dashed), and 10^4 (dot-dashed) particle SPH impacts simulations as a function of run time due to spreading associated with the code's artificial viscosity treatment.

4.3. General outcomes

Table 1 shows results from the simulations described above. Fig. 15 compares final disk and system properties produced in simulations with CTH and SPH, including those discussed above and four additional CTH simulations. For the latter, results are shown at $t = 30$ h and there is no significant mass loss from the grid. While there is substantial scatter, the values obtained are broadly consistent with those found previously (e.g., Canup, 2008, Figs. 1 and 7; Reufer et al., 2012). The CTH disks are generally somewhat less massive and less radially extended (i.e., smaller average j_{disk}) than their SPH counterparts. For the cases studied here, disk masses range from 1.1 to $2M_L$, and the fraction of the disks originating from the target ranges from 0.1 to 0.7.

Fig. 15f shows the predicted mass of the Moon that would accrete from each disk from Eq. (1) vs. the final bound angular momentum of the planet-disk system produced by each impact.

5. Discussion

To assess whether changes in resolution or numerical method affect the mass, angular momentum, and provenance of material

in the protolunar disk, we have performed the first direct comparison between lunar-forming impact simulations performed with both an Eulerian (AMR-CTH) and a Lagrangian (SPH) code. We have also tested the effect of varying resolutions with both methods on impact outcome. We focus primarily on successful candidate impacts involving low-velocity, oblique impacts by an impactor containing between 13 and 20% of the Earth's mass (e.g., Canup and Asphaug, 2001; Canup, 2004a, 2008), but we also consider a recently proposed scenario involving a higher-velocity, less oblique impact (Reufer et al., 2011, 2012).

The properties of the post-impact protolunar disk calculated by each hydrocode impact simulation are time-dependent. Ideally, one desires a sufficiently long simulation to provide an accurate estimate of the disk properties while also minimizing artificial numerical effects that accumulate with time. To accurately describe the disk's mass requires that large intact clumps that exist after the initial impact, which often contain of order tens of percent or more of a lunar mass and have periapses within the Roche limit, be simulated for at least one orbit to account for tidal disruption events. This typically requires a ~ 25 – 50 h simulation. For current resolutions and techniques, some artificial evolution of the disk properties due to numerical effects will occur during this period. For SPH, the large smoothing lengths of disk particles produce an artificial viscosity that spreads the disk at an artificially rapid rate, with a characteristic disk spreading timescale of $\sim 10^2$ to a few $\times 10^2$ h. We estimate (Appendix B) this leads to an artificial decrease in the disk mass of up to $\sim 10\%$, and to an artificial increase in the disk's specific angular momentum of up to a few percent, during our typical SPH simulations. For extended CTH simulations, it is possible for material to flow out of the grid. In most of our CTH simulations, this is only a minor effect, although in our longest, 80-h simulation (Section 4.2.2) $\sim 0.14M_L$ is lost at late times, which likely artificially reduces the disk mass in that case.

We find that both CTH and SPH produce similar predictions for the orbiting mass and its angular momentum for the first few hours after the initial impact at all of the resolutions considered here. This suggests that the primary impact event is well resolved. Results often begin to substantially diverge after about 5–10 h post-impact, as the evolution of the system becomes dominated by the specific orbits and masses of individual large clumps. Results generally re-converge to within tens of percent when simulations are continued until all of the large clumps on unstable orbits (i.e., those that will re-impact the Earth or pass well within the Roche limit and be disrupted) have completed at least one orbit. Our final CTH disks have masses and angular momenta that are typically $\sim 10\%$ less than the disks produced by SPH simulations of comparable impacts. This appears to be due to inherent differences between the codes. For simulations using the same method but varied resolutions, the disk mass varies stochastically with a standard deviation of about 10–20%.

The majority of protolunar disk material originates from the impactor rather than from the protoearth for low-velocity, oblique impacts. This result does not appear to be systematically affected by either numerical method or resolution. Consideration of pre-impact retrograde rotation in the target can increase the percentage of target material in the disk for these types of impacts to 40–50% (Canup, 2008 and Section 4.6). Such cases are favorable candidates because they can also produce massive disks and a close match to the Earth–Moon system angular momentum (Canup, 2008; Fig. 15f). Reufer et al. (2011, 2012) have proposed that a less oblique, higher-velocity collision can produce a disk derived predominantly from the target. For the specific case advocated by Reufer et al. (2011), we find that the fraction of the disk originating from the target is indeed higher, ~ 50 – 70% (Section 4.8), similar

to the $\sim 60\%$ target disk for this case found by Reufer et al. (2011, 2012).

Having a substantial fraction of the protolunar disk originate from the impactor must ultimately be reconciled with the identical O-isotope compositions of the Earth and Moon (e.g., Wiechert et al., 2001). One possibility is that extensive mixing between protolunar and protoearth material after the impact but prior to the Moon's formation allowed compositions to equilibrate (Pahlevan and Stevenson, 2007). The mixing scenario appears to require that the Moon's formation be delayed by about a hundred years or more after the impact. Improved models of protolunar disk evolution and lunar accretion will be needed to assess whether this is plausible. In particular, material on orbits entirely exterior to the Roche limit will likely accrete rapidly and may have little opportunity to compositionally equilibrate with the Earth via vapor exchange in the Roche interior disk (Salmon and Canup, 2012). In our simulations here, the percentage of the disk mass that orbits entirely exterior to the Roche limit ranges from $\sim 10\%$ to 80% , with a mean of about 40%.

Acknowledgments

The authors thank H.J. Melosh and E. Asphaug for detailed and helpful reviews. R.M.C. was supported by NASA's LASER program and the NASA Lunar Science Institute (NLSI); A.C.B. acknowledges support from NLSI. D.A.C. is an employee of Sandia, a multiprogram laboratory operated by Sandia Corporation, a Lockheed Martin Company, for the United States Department of Energy under Contract DE-AC04-94AL85000.

Appendix A. Dunitite Equation of State (EOS) for CTH 9.1

All our simulations use M-ANEOS for the mantle material, and ANEOS for the iron cores of the impactors and targets. Our SPH simulations consider a dunitite (forsterite) mantle, using the same M-ANEOS coefficients as used in prior SPH simulations (Canup, 2004a, 2008). We here also developed a modified dunitite EOS for the specific EOS structure contained in CTH that matches as closely as possible that used in the SPH simulations, as described next. These parameters are contained in Table A1.

Key changes to the equation of state to treat molecules arise in the “cold” term of the ANEOS equation of state, which describes the behavior of the material at densities much larger than the reference density at zero temperature, and also at extremely low densities.

In the atomic EOS, the parameter E_{sep} was used to describe the energy required to separate the atoms from each other. In the molecular version, this parameter is used to describe the energy to vaporize the material, $E_{vap} = 1.3 \times 10^{11}$ erg g^{-1} . This controls, in part, the critical point. M-ANEOS also includes a modification to the inter-atomic potential. Rather than using the Morse or Lennard–Jones potentials available in ANEOS, the updated version uses what Melosh refers to as “Mie-type” potential (of which Lennard–Jones is a specific case), where $P_{cold} = C(\eta^m - \eta^a)$ and $0 < \eta < 1$ (cf. Eq. 4 in Melosh, 2007), where $m > a$ to assure P_{cold} is tensional, and η is the compression. The constants C and m are determined from the vaporization energy (related to the integral of P_{cold}), and continuity of $dP_{cold}/d\eta$ at $\eta = 1$, where P_{cold} is matched between compressed and non-compressed states. Various exponents $1.2 < a < 3.0$ may be substituted into the equation (Melosh, 2007), and affect the behavior of the interatomic potential at large distances. Melosh (2007) advocates a value of $a = 1.7$ for quartz, but $a = 1.27$ is used here for consistency with the form of the equation of state used in our SPH simulations. A value of $a = 4/3$ is appropri-

ate for a solid bound by Coulomb forces, $a = 7/3$ corresponds to a solid bound by Van Der Waals forces, and also the well-known Lennard–Jones 6–12 interatomic potential. Different values of a shift the critical point and affect the slope of the liquid/vapor phase curve.

The second group of changes to ANEOS involve changes to the Helmholtz free energy due to the partitioning of energy in a molecular gas. Melosh (2007) includes rotational and vibrational contributions to the free energy, but these terms are not included here for consistency with the EOS used in the SPH simulations. Without these terms, the partition function for the molecular gas is $f_c = (1/\rho) (2\pi m_c kT/h^2)^{3/2} \exp(E_b/kT)$, where m_c is the cluster mass, E_b is the binding energy, k is Boltzman's constant, T is temperature and ρ is density (Melosh, 2007).

We performed a small adjustment to the critical point using built-in adjustment equations in ANEOS governed by parameters c_{53} and c_{54} . For $\eta < c_{54}$, the interatomic potential and energy terms are adjusted in an amount proportional to c_{53} (see Eqs. (3.33) and (3.34) in Thompson and Lauson, 1972). We use a value of $c_{54} = 0.8$ following Melosh (see also Appendix E of Thompson and Lauson, 1972), and adjust the value of c_{53} until the critical pressure matches the desired value.

With these modifications, we are able to obtain a dunite EOS for CTH that matches that used in prior SPH simulations quite closely.

Appendix B. Effect of numerical spreading on disk properties

In the continuum limit as the smoothing length $h \rightarrow 0$, the SPH linear artificial viscosity term generates an effective kinematic viscosity $\nu = \bar{\alpha}ch/8$, where $\bar{\alpha} = 1.5$ is the code's linear viscosity parameter, c is the sound speed, and h is the characteristic particle smoothing length (Murray, 1996; Nelson et al., 1998). This expression for ν has been verified (Murray, 1996) through direct comparison of SPH simulations of the expansion of an axisymmetric ring with viscosity ν with semi analytic solutions of Lynden-Bell and Pringle (1974).

We here crudely estimate the effect of spreading due to the code's artificial viscosity on the protolunar disk's properties during a typical 20–50 h giant impact simulation. We consider a idealized disk diffusion model (developed by W.R. Ward and utilized in Ward and Canup, 2000, and Salmon and Canup, 2012) that assumes a uniform surface density between an inner radius R and an outer edge at radius r_d , with $x \equiv r_d/R$. Viscous spreading increases the disk width, $w = r_d - R$, on a time $t_v = w^2/\nu$; differentiating with respect to time gives

$$(\dot{r}_d - \dot{R}) = \frac{\nu}{2(r_d - R)} \quad (\text{A1})$$

The disk angular momentum is $L = 4/5M_d\sqrt{GM_pR}[(x^{5/2} - 1)/(x^2 - 1)]$, where M_d is the disk's mass. Viscosity transports angular momentum but produces no net torque on the disk, and setting $dL/dt = 0$ gives

$$\dot{R} = f(x)\dot{r}_d$$

$$f(x) \equiv \frac{2x(x^{5/2} - 1) - 5/2x^{3/2}(x^2 - 1)}{2(x^{5/2} - 1) - 5/2(x^2 - 1)} \quad (\text{A2})$$

Combining (A1) and (A2) gives

$$\dot{r}_d = \frac{\nu}{2R(x-1)(1-f(x))} \quad (\text{A3})$$

We now set R to be the surface of the planet. The change in the disk mass due to the viscous transport of mass inward onto the planet is

$$\frac{dM_d}{dt} = 2\pi R \dot{r}_d \sigma = \frac{2RR\dot{M}_d}{R^2(x^2 - 1)} \quad (\text{A4})$$

Eqs. (A2)–(A4) define the evolution of M_d and r_d with time as a uniform surface density disk spreads with viscosity ν .

We use this simplified approach to track the evolution of a disk with an initial outer edge $r_d = 5R$ and a specific angular momentum comparable to most of the disks produced here, which typically have $J_{\text{disk}} \sim 1$. To estimate ν , we use representative mass-weighted values from the disks in our SPH simulations, specifically $\langle c \rangle = 2 \text{ km s}^{-1}$, with $\langle h \rangle = 3000 \text{ km}$, 6500 km , and $14,000 \text{ km}$ for the 10^6 , 10^5 , and 10^4 particle simulations, respectively (our simulations imposed an upper limit of $h = 500,000 \text{ km}$, which generally applies only to the most distant disk particles). We calculate the change in the disk mass with time due to accretion onto the Earth, and the associated change in the disk's specific angular momentum as M_D is reduced and the disk's outer edge viscously expands. Fig. B1 shows the estimated fractional decrease in M_D and the fractional increase in J_D as a function of time estimated for the three resolutions. These estimates should be broadly illustrative but will be only coarsely accurate, given our simplified disk model and that $\langle c \rangle$ and $\langle h \rangle$ vary from case-to-case even for a fixed resolution. Fig. B1 implies that numerical spreading has relatively minimal effect on disk properties for $N > 10^4$ for $t < 10 \text{ h}$. However, the simulations must typically be tracked for $\sim 25\text{--}50 \text{ h}$ in order to allow large intact clumps with periapses interior to the Roche limit to complete at least one orbit. For these run times and $10^5 \leq N \leq 10^6$, artificial viscosity is expected to decrease the disk mass by $\sim 5\text{--}10\%$, while the specific angular momentum is artificially increased by a few percent. The predicted mass of the Moon from Eq. (1) is not substantially affected by numerically induced spreading.

References

- Agnor, C.B., Asphaug, E., 2004. Accretion efficiency during planetary collisions. *Astrophys. J.* 613, L157–L160.
- Agnor, C.B., Canup, R.M., Levison, H.F., 1999. On the character and consequences of large impacts in the late stage of terrestrial planet formation. *Icarus* 142, 219–237.
- Asphaug, E., 2010. Similar-sized collisions and the diversity of planets. *Chem. Erde – Geochem.* 70, 199–219.
- Balsara, D., 1995. Von Neumann stability analysis of smooth particle hydrodynamics—suggestions for optimal algorithms. *J. Comput. Phys.* 121, 357–372.
- Barnes, J., Hut, P., 1986. A hierarchical O(N log N) force-calculation algorithm. *Nature* 324, 446–449.
- Belbruno, E., Gott III, R.J., 2005. Where did the Moon come from? *Astron. J.* 129, 1724–1745.
- Benz, W., Slattery, W.L., Cameron, A.G.W., 1986. The origin of the Moon and the single impact hypothesis I. *Icarus* 66, 515–535.
- Benz, W., Slattery, W.L., Cameron, A.G.W., 1987. The origin of the Moon and the single impact hypothesis II. *Icarus* 71, 30–45.
- Benz, W., Cameron, A.G.W., Melosh, H.J., 1989. The origin of the Moon and the single impact hypothesis III. *Icarus* 81, 113–131.
- Cameron, A.G.W., Ward, W.R., 1976. The origin of the Moon. *Lunar Planet. Sci.* VII, 120–122.
- Canup, R.M., 2004a. Simulations of a late lunar forming impact. *Icarus* 168, 433–456.
- Canup, R.M., 2004b. Dynamics of lunar formation. *Ann. Rev. Astron. Astrophys.* 42, 441–475.
- Canup, R.M., 2008. Lunar-forming collisions with pre-impact rotation. *Icarus* 196, 518–538.
- Canup, R.M., Asphaug, E., 2001. Origin of the Moon in a giant impact near the end of the Earth's formation. *Nature* 412, 708–712.
- Canup, R.M., Barr, A.C., 2010. Modeling Moon-forming impacts: High-resolution SPH and CTH simulations. *Lunar Planet. Sci.* XXXXI, 2488.
- Canup, R.M., Ward, W.R., Cameron, A.G.W., 2001. A scaling relationship for satellite-forming impacts. *Icarus* 150, 288–296.
- Canup, R.M., Asphaug, E., Pierazzo, E., Melosh, H.J., 2002. Simulations of Moon-forming impacts. *Lunar Planet. Sci.* XXXIII, 1641.
- Chambers, J.E., Wetherill, G.W., 1998. Making the terrestrial planets: N-body integrations of planetary embryos in three dimensions. *Icarus* 136, 304–327.
- Crawford, D.A., 2011a. CTH simulations of candidate Moon forming impacts. *Lunar Planet. Sci.* XXXII.
- Crawford, D.A., 2011b. Parallel N-body gravitational interaction in CTH for planetary defense and large impact simulations. In: *Proc. 11th Hypervel. Impact Sympos.*, p. 155 (abstract).

- Crawford, D.A., Kipp, M.E., 2010. Giant impact theory for origin of the Moon: High resolution CTH simulations. *Lunar Planet. Sci.* XXXXI, 1405.
- Crawford, D.A., Taylor, P.A., Bell, R.L., Hertel, E.S., 2006. Adaptive mesh refinement in the CTH shock physics hydrocode. *Russ. J. Phys. Chem. B* 25 (9), 85–90.
- Ćuk, M., Stewart, S.T., 2012. Despinning of Earth by Moon–Sun orbital resonance. *Early Solar System Impact Bombardment II*, February 1–3, Houston, TX.
- Desch, S., Taylor, J., 2011. A model of the Moon's volatile depletion. *Lunar Planet. Sci.* XXXXII, 2005.
- Georg, R.B., Halliday, A.N., Schauble, E., Reynolds, B.C., 2007. Silicon in the Earth's core. *Nature* 447, 1102–1106.
- Goldreich, P., Ward, W.R., 1973. The formation of planetesimals. *Astrophys. J.* 183, 1051–1062.
- Hauri, E., Weinreich, T., Saal, A.E., Rutherford, M.C., Van Orman, J.A., 2011. High pre-eruptive water contents preserved in lunar melt inclusions. *Science* (published online 26 May).
- Ida, S., Canup, R.M., Stewart, G.R., 1997. Lunar accretion from an impact generated disk. *Nature* 389, 353–357.
- Imaeda, Y., Inutsuka, S., 2002. Shear flows in smoothed particle hydrodynamics. *Astrophys. J.* 569, 501–518.
- Kokubo, E., Makino, J., Ida, S., 2000. Evolution of a circumterrestrial disk and formation of a single Moon. *Icarus* 148, 419–436.
- Leinhardt, Z.M., Stewart, S.T., 2012. Collisions between gravity-dominated bodies. I. Outcome regimes and scaling laws. *Astrophys. J.* 745, 79–106.
- Lynden-Bell, D., Pringle, J.E., 1974. The evolution of viscous discs and the origin of the nebular variables. *Mon. Not. Royal Astron. Soc.* 168, 603–637.
- McGlaun, J.M., Thompson, S.L., Elrick, M.G., 1990. CTH: A 3-dimensional shock-wave physics code. *Int. J. Imp. Eng.* 10, 351–360.
- Melosh, H.J., 2007. A hydrocode equation of state for SiO₂. *Meteor. Planet. Sci.* 42, 2079–2098.
- Melosh H.J., Kipp, M.E., 1989. Giant impact theory of the Moon's origin: First 3D Hydrocode results. *Lunar Planet. Sci.* XX, 685–686.
- Murray, J.R., 1996. SPH simulations of tidally unstable accretion discs in cataclysmic variables. *Mon. Not. Roy. Astron. Soc.* 279, 402–414.
- Nelson, A.F., Benz, W., Adams, F.C., Arnett, D., 1998. Dynamics of circumstellar disks. *Astrophys. J.* 502, 342–371.
- Pahlevan, K., Stevenson, D., 2007. Equilibration in the aftermath of the lunar-forming giant impact. *Earth Planet. Sci. Lett.* 262, 438–449.
- Pahlevan, K., Stevenson, D., Eiler, J.M., 2011. Chemical fractionation in the silicate vapor atmosphere of the Earth. *Earth Planet. Sci. Lett.* 301, 433–443.
- Pierazzo, E., Vickery, A.M., Melosh, H.J., 1997. A reevaluation of impact melt production. *Icarus* 127, 408–423.
- Pierazzo, E., Artemieva, N., Asphaug, E., Baldwin, E.C., Cazamias, J., Coker, R., Collins, G.S., Crawford, D.A., Davison, T., Elbeshhausen, D., Holsapple, K.A., Housen, K.R., Korycansky, D.G., Wünnemann, K., 2008. Validation of numerical codes for impact and explosion cratering: Impacts on strengthless and metal targets. *Meteor. Planet. Sci.* 43, 1917–1938.
- Reufer, A., Meier, M., Benz, W., Wieler, R., 2011. Obtaining higher target material proportions in the giant impact by changing impact parameters and impactor composition. *Lunar Planet. Sci.* XXXXII, 1136.
- Reufer, A., Meier, M.M.M., Benz, W., Wieler, R., 2012. A hit-and-run giant impact scenario. *Icarus* 212, 296–299.
- Saal, A.E. et al., 2008. Volatile content of the lunar volcanic glasses and the presence of water in the Moon's interior. *Nature* 454, 192.
- Salmon, J., Canup, R.M., 2012. Three-stage lunar accretion: Slow growth of the Moon and implications for Earth–Moon isotopic similarities. *Lunar Planet. Sci.* XXXXIII, 2540.
- Steinmetz, M., Müller, E., 1993. On the capabilities and limits of smoothed particle hydrodynamics. *Astron. Astrophys.* 268, 391–410.
- Thompson, S.L., Lauson, H.S., 1972. Improvements in the Chart-D radiation hydrodynamic code III: Revised analytical equation of state. Technical Rep. SC-RR-710714 (Sandia Nat. Labs).
- Thompson, C., Stevenson, D.J., 1988. Gravitational instability in two-phase disks and the origin of the Moon. *Astrophys. J.* 333, 452–481.
- Touboul, M., Kleine, T., Bourdon, B., Palme, H., Wieler, R., 2007. Late formation and prolonged differentiation of the Moon inferred from W isotopes in lunar metals. *Nature* 450, 1206–1209.
- Touma, J., Wisdom, J., 1998. Resonances in the early evolution of the Earth–Moon system. *Astron. J.* 115, 1653–1663.
- Wada, K., Kokubo, E., Makino, J., 2006. High-resolution simulations of a Moon-forming impact and postimpact evolution. *Astrophys. J.* 638, 1180–1186.
- Ward, W.R., Cameron, A.G.W., 1978. Disc evolution within the Roche limit. *Lunar Planet. Sci.* IX, 1205–1207.
- Ward, W.R., Canup, R.M., 2000. Origin of the Moon's inclination from resonant disk interactions. *Nature* 403, 741–743.
- Wiechert, U., Halliday, A.N., Lee, D.C., Synder, G.A., Taylor, I.A., Rumble, D., 2001. Oxygen isotopes and the Moon-forming giant impact. *Science* 294, 345–348.